J. Fluid Mech. (2022), *vol*. 939, A1, doi:10.1017/jfm.2021.1031

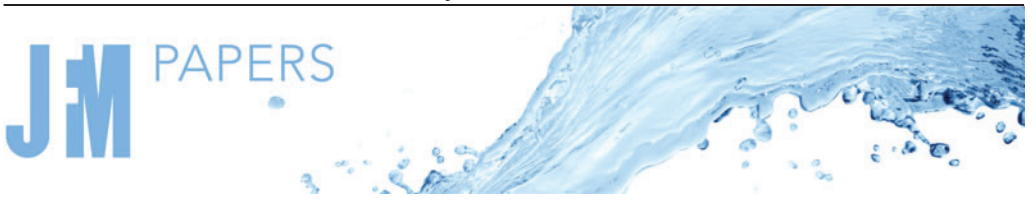

Multiple heat transport maxima in confined-rotating Rayleigh–Bénard convection

Robert Hartmann[1],†, Roberto Verzicco[1,2,3], Liesbeth Klein Kranenbarg[1], Detlef Lohse[1,4] and Richard J.A.M. Stevens[1]

[1]Physics of Fluids Group and Max Planck Center for Complex Fluid Dynamics, Mesa+ Institute, and J.M. Burgers Center for Fluid Dynamics, University of Twente, P.O. Box 217, 7500 AE Enschede, The Netherlands

[2]Dipartimento di Ingegneria Industriale, University of Rome 'Tor Vergata', Via del Politecnico 1, Roma 00133, Italy

[3]Gran Sasso Science Institute, Viale F. Crispi, 7, 67100 L'Aquila, Italy

[4]Max Planck Institute for Dynamics and Self-Organisation, Am Fassberg 17, 37077 Göttingen, Germany

(Received 3 July 2021; revised 14 October 2021; accepted 15 November 2021)

Moderate rotation and moderate horizontal confinement similarly enhance the heat transport in Rayleigh–Bénard convection (RBC). Here, we systematically investigate how these two types of flow stabilization together affect the heat transport. We conduct direct numerical simulations of confined-rotating RBC in a cylindrical set-up at Prandtl number $Pr = 4.38$, and various Rayleigh numbers $2 \times 10^8 \leqslant Ra \leqslant 7 \times 10^9$. Within the parameter space of rotation (given as inverse Rossby number $0 \leqslant Ro^{-1} \leqslant 40$) and confinement (given as height-to-diameter aspect ratio $2 \leqslant \Gamma^{-1} \leqslant 32$), we observe three heat transport maxima. At lower Ra, the combination of rotation and confinement can achieve larger heat transport than either rotation or confinement individually, whereas at higher Ra, confinement alone is most effective in enhancing the heat transport. Further, we identify two effects enhancing the heat transport: (i) the ratio of kinetic and thermal boundary layer thicknesses controlling the efficiency of Ekman pumping, and (ii) the formation of a stable domain-spanning flow for an efficient vertical transport of the heat through the bulk. Their interfering efficiencies generate the multiple heat transport maxima.

Key words: Bénard convection, rotating turbulence, rotating flows

† Email address for correspondence: r.hartmann@utwente.nl

1. Introduction

Rayleigh–Bénard convection (RBC) (e.g. Ahlers, Grossmann & Lohse 2009; Lohse & Xia 2010; Chilla & Schumacher 2012) is the paradigmatic model system to study thermal or buoyancy-driven flows. In reality, most convective systems deviate substantially from the ideal RBC model owing to one or more stabilizing factors. For example, the fluid layer must obviously be confined in the lateral directions for technical applications, background rotation is omnipresent in astro- and geophysics (e.g. Glatzmaier & Roberts 1995; Hartmann, Moy & Fu 2001; Heimpel, Aurnou & Wicht 2005; Aurnou *et al.* 2015), and the additional contribution of salinity to buoyancy sets up double-diffusive convection in oceanography (e.g. Schmitt *et al.* 2005; Timmermans *et al.* 2008; Radko 2013). Chong *et al.* (2017) have shown by direct comparison that these different types of stabilization affect the heat transport of the system similarly: for moderate flow stabilization, the heat transport is enhanced compared with the heat transport in the non-stabilized system. On the contrary, when the stabilizing forcing is strong compared with the driving buoyancy, the heat transport is reduced and eventually suppressed. Still, most studies have focused on investigating each of the stabilizing effects separately. This study investigates the heat transport enhancement when two types of stabilization, namely rotation and horizontal confinement, are present simultaneously.

Confined-rotating RBC is fully controlled by four dimensionless parameters: the Prandtl number Pr describing the fluid properties, the Rayleigh number Ra setting the strength of thermal driving, the inverse Rossby number Ro^{-1} as a measure of the rotation rate and the height-to-width aspect ratio Γ^{-1} defining the horizontal confinement of the domain (complete definitions in § 2). Note that, for convenience, we will use the inverse Rossby number Ro^{-1} and the confinement parameter Γ^{-1} throughout the paper, such that the case ($Ro^{-1} = 0$, $\Gamma^{-1} = 0$) characterizes the classical non-stabilized RBC system. The global response of the system is expressed in the Nusselt number Nu, describing the dimensionless heat transport from the bottom to the top plate, and the directional Reynolds numbers Re_i as a measure for the strength of motion in the different directions i (full definitions in § 2).

Several stabilizing effects and mechanisms have been observed in rotating RBC and confined RBC. In general, the stabilizing character of both confinement and rotation increases the critical Rayleigh number Ra_c that is needed to initiate convection (Chandrasekhar 1961). By increasing rotation Ro^{-1} or confinement Γ^{-1} at fixed Ra, rotating RBC or confined RBC traverses various flow regimes towards a non-convective state. We now describe these regimes in more detail, beginning with rotating RBC.

In the absence of rotation ($Ro^{-1} = 0$) and for slow rotation ($Ro^{-1} \ll 1$), thermal buoyancy is the dominating force in the momentum balance. In this buoyancy-dominated regime, the flow dynamics and heat transport are mostly unaffected by the rotation, and often a large-scale background circulation is present (e.g. Brown, Nikolaenko & Ahlers 2005; van der Poel *et al.* 2015). Accordingly, we expect vertical motion to be larger than horizontal motion in the buoyancy-dominated regime ($Re_z > Re_H$).

For moderate rotation ($Ro^{-1} \approx 1$), when the Coriolis force and the buoyancy force make a similar contribution, the large-scale circulation is replaced by vertically aligned vortices (e.g. Vorobieff & Ecke 1998; Kunnen, Clercx & Geurts 2008). Counterintuitively to the increasing flow stabilization, the heat transport can be significantly enhanced as compared with the non-rotating case for a system with $Pr > 1$ (e.g. Kunnen, Clercx & Geurts 2006; Zhong *et al.* 2009). The heat transport enhancement results from Ekman pumping feeding the vortices with hot or cold fluid from the boundary layers (e.g. Rossby 1969).

Theoretically, the enhancement by Ekman pumping is most efficient when the kinetic and thermal boundary layer thicknesses are equal (Stevens, Clercx & Lohse 2010*b*; Yang *et al.* 2020), which, however, is only observed up to a certain Ra (Yang *et al.* 2020).

For rapid rotation ($Ro^{-1} \gg 1$), when the Coriolis force largely surpasses the buoyancy force, the flow dynamics is mainly controlled by the geostrophic balance. In this geostrophic (or rotation-dominated) regime, vertical motion is further suppressed (Proudman 1916; Taylor & Lamb 1917) and the heat transport decreases rapidly with increasing rotation (e.g. Ecke & Niemela 2014). Nonetheless, Ekman pumping remains important for heat transport (Stellmach *et al.* 2014). Different types of flow organization have been observed within the geostrophic regime, depending on Ra and Pr (e.g. Sprague *et al.* 2006; Julien *et al.* 2012; Nieves, Rubio & Julien 2014; Stellmach *et al.* 2014): the flow can either still organize in vertically coherent structures (e.g. convective Taylor columns) or settle into vertically decorrelated geostrophic turbulence. Moreover, Zhang *et al.* (2020) and de Wit *et al.* (2020) recently discovered boundary zonal flow in finite-size cylinders, which can make a significant contribution to the heat transport (Lu *et al.* 2021; Zhang, Ecke & Shishkina 2021). This already depicts an interplay of confinement and rotation.

In both the moderately rotating and the geostrophic regime, vortical structures dominate the flow. Hence, we expect horizontal motion to be larger than vertical motion ($Re_H > Re_z$). In the context of this paper, we refer to both together as the rotation-controlled regime as the direct counterpart of the buoyancy-dominated regime. Accordingly, we will use $Re_z = Re_H$ as our definition to describe the transition between the two regimes. We note that various definitions for this transition and the corresponding transitional Rossby number $Ro^{-1}_{BD\text{-}RC}$ have been used in literature based on different characteristics, when (i) the kinetic boundary layer changes from Prandtl–Blasius type to Ekman type (Stevens *et al.* 2009; Stevens, Clercx & Lohse 2010*a*; Kunnen *et al.* 2011; Rajaei *et al.* 2016*a*), (ii) the flow dynamics changes from a large-scale circulation to vertically aligned vortices (Julien *et al.* 1996; Kunnen *et al.* 2008; Rajaei *et al.* 2016*b*) and (iii) heat transport enhancement sets in (Stevens *et al.* 2009; Weiss *et al.* 2010). However, several recent studies have revealed a more detailed view of this transition (Weiss & Ahlers 2011*a*; Stevens, Clercx & Lohse 2013*a*; Weiss, Wei & Ahlers 2016), and have shown that the different characteristics are related to similar, but slightly different rotation rates within a narrow interval of Ro^{-1} (Wei, Weiss & Ahlers 2015; Alards *et al.* 2019).

Finally, beyond a critical rotation rate ($Ro^{-1} > Ro_c^{-1}$), the amount of thermal driving does not suffice to initiate convection ($Ra < Ra_c(Ro^{-1})$), and the heat transport is purely conductive. In finite-size systems, an additional regime of wall-mode convection is observed for $Ro^{-1} > Ro_c^{-1}$ (e.g. Buell & Catton 1983; Zhong, Ecke & Steinberg 1991; Liu & Ecke 1997; Favier & Knobloch 2020). Therein, the bulk is already in rest, but weak convective flow is generated next to the sidewalls, which results in a heat transport larger than conduction. This again depicts an interplay of confinement and rotation.

Analogue regimes in terms of the heat transport also exist in confined RBC (Chong *et al.* 2015; Chong & Xia 2016). In domains with a large horizontal extent ($\Gamma^{-1} \ll 1$) the flow is controlled by the boundary layers as in classical RBC (Chong *et al.* 2015). In this regime, the heat transport is mostly insensitive to Γ^{-1} and adapts the value from the unconfined case. By reducing the horizontal extent the flow first enters a plume-controlled regime for moderate confinement ($\Gamma^{-1} \gtrsim 1$), in which the heat transport is enhanced, before, in the severely confined regime ($\Gamma^{-1} \gg 1$), the heat transport is strongly reduced (Chong *et al.* 2015; Chong & Xia 2016). Finally, the system becomes too confined to initiate convection $Ra_c(\Gamma^{-1}) > Ra$ (e.g. Chandrasekhar 1961; Catton & Edwards 1970; Chong & Xia 2016;

Ahlers *et al.* 2022). Similar to the rotation-controlled regime in rotating RBC, vertically coherent structures form within the plume-controlled regime in confined RBC (Chong *et al.* 2015; Hartmann *et al.* 2021). Contrary to the studies of Chong *et al.* (2015, 2017) and Chong & Xia (2016), the present study deals with cylindrical confinement. Hartmann *et al.* (2021) have shown that heat transport enhancement in confined RBC generally occurs in cylindrical and cuboid domains, but flow organization, optimal confinement Γ^{-1} and amplitude of heat transport enhancement are strongly influenced by the cell geometry. Further, Zwirner & Shishkina (2018) have shown that an inclined gravity in addition to confinement is able to significantly enhance the heat transport.

Chong *et al.* (2017) have nicely revealed more striking similarities in heat transport enhancement for individually examined types of stabilization: confinement, rotation and an additional stabilizing buoyant scalar field as in double-diffusive convection. These similarities lead to the question of how multiple types of stabilization exactly interplay with each other, whether their effects simply superpose or complexly interact. By direct numerical simulations (DNSs) of confined-rotating RBC in a cylindrical set-up (§ 2), we explore the two-dimensional parameter space of Ro^{-1} and Γ^{-1} at fixed Ra and Pr to identify the maxima of heat transfer (§ 3), elucidate the governing effects and mechanisms and discuss their interaction (§ 4). Finally, we will compare the results from different Ra and discuss their implications (§ 5).

2. Numerical set-up and analysis methods

We perform DNSs of RBC in a cylindrical sample rotating around its vertical axis. The governing equations in RBC encompass the balances of mass, momentum and energy conservation. The influence of constant rotation around the axis is included by considering the Coriolis force in the momentum equations. For an incompressible fluid the governing equations under the Oberbeck–Boussinesq approximation are solved in their dimensionless form (e.g. Zhong *et al.* 2009)

$$\left.\begin{gathered}\boldsymbol{\nabla}\cdot\boldsymbol{u}=0\\ \frac{\mathrm{d}\boldsymbol{u}}{\mathrm{d}t}=-\boldsymbol{\nabla}P+\sqrt{\frac{Pr}{Ra}}\nabla^2\boldsymbol{u}+\Theta\boldsymbol{e}_z-\frac{1}{Ro}\boldsymbol{e}_z\times\boldsymbol{u}\\ \frac{\mathrm{d}\Theta}{\mathrm{d}t}=\frac{1}{\sqrt{Pr\,Ra}}\nabla^2\Theta.\end{gathered}\right\}\tag{2.1a–c}$$

Here, $\boldsymbol{u}$, P and Θ are the normalized velocity, pressure and temperature fields, respectively. The equations are normalized by the height of the cylinder H and the free-fall velocity $U_0=\sqrt{\alpha g\Delta T H}$, where α is the isobaric thermal expansion coefficient, g the gravitational acceleration and ΔT the temperature difference between upper and lower plate. The temperature is normalized as $\Theta=(T-T_{top})/\Delta T\in[0,1]$. The pressure field P is reduced by the hydrostatic balance and centrifugal contributions. The control parameters in the equations then are the Prandtl number Pr, the Rayleigh number Ra and the inverse Rossby number Ro^{-1}

$$Pr=\nu/\kappa;\quad Ra=\alpha g\Delta T H^3/(\nu\kappa);\quad Ro^{-1}=2\Omega H/U_0.\tag{2.2a–c}$$

Here, ν is the kinematic viscosity, κ the thermal diffusivity and Ω the rotation rate. The inverse Rossby number Ro^{-1} can alternatively be expressed in terms of the Ekman number

Ek: $Ro^{-1} = 2\sqrt{Pr/Ra}\,Ek^{-1}$. Finally, the confinement parameter Γ^{-1} defines the cylinder size of height H and diameter D:

$$\Gamma^{-1} = H/D. \tag{2.3}$$

No-slip boundary conditions are imposed on the isothermal top and bottom plates and the adiabatic sidewall. In all simulations the Prandtl number is fixed at $Pr = 4.38$ ($\approx$ water), the Rayleigh number is chosen in the range $2 \times 10^8 \leqslant Ra \leqslant 7 \times 10^9$. Among all Ra we cover a parameter space of $0 \leqslant Ro^{-1} \leqslant 40$ and $2 \leqslant \Gamma^{-1} \leqslant 32$.

The governing equations (2.1) are solved by a central second-order accurate finite-difference discretization on a staggered grid as presented in Verzicco & Orlandi (1996) and Verzicco & Camussi (1997, 1999). The code has been often validated (e.g. Kooij *et al.* 2018). For a sufficient resolution of the Kolmogorov scales in the entire domain, we increase the number of grid points in the vertical direction from $N_z = 256$ for $Ra = 2 \times 10^8$ up to $N_z = 768$ for $Ra = 7 \times 10^9$. Additionally, we use a stretched grid in the vertical and radial directions to ensure that the resolution of the boundary layers at the plates and the sidewall fulfil the required criteria given in Shishkina *et al.* (2010). The dynamic time stepping in our simulations is controlled by a maximum Courant number and a maximum time step. The numerical parameters per simulation set are summarized in Appendix A.

The global key response parameter of the system is the dimensionless heat transport given by the Nusselt number $Nu = QH/(\kappa \Delta T)$ with the heat flux Q from the bottom to the top plate. We compute $Nu \equiv \langle Nu(t) \rangle_t$ directly from the vertical gradient of the dimensionless temperature Θ as the average $\langle \cdot \rangle$ over both plates

$$Nu(t) = \left\langle -\partial_z \left\langle \Theta(t) \right\rangle_{r,\vartheta} \right\rangle_{z=\{0,1\}}. \tag{2.4}$$

For comparison between different Ra, we present all heat transport data normalized as Nu/Nu_0, where $Nu_0(Ra, Ro^{-1} = 0, \Gamma^{-1} = 1)$ serves as Ra-dependent reference value of the (mostly) non-stabilized system, i.e. a non-rotating, sufficiently wide cylinder. The reference values Nu_0 are known from various experiments and numerical simulations, and are well described by the Grossmann–Lohse theory (Grossmann & Lohse 2000, 2001; Stevens *et al.* 2013*b*). Further, we use the root mean square (r.m.s.) of the normalized temporal Nusselt number fluctuations to quantify the temporal stability of the flow

$$Nu_{rms} = \sqrt{\left\langle \left(\frac{Nu(t)}{\langle Nu \rangle_t} - 1 \right)^2 \right\rangle_t}. \tag{2.5}$$

To characterize the flow we use the directional Reynolds numbers $Re_{r,\vartheta,z} \equiv \left\langle Re_{r,\vartheta,z}(t) \right\rangle_t$ based on the dimensionless r.m.s. velocities $\sqrt{\left\langle u_i^2 \right\rangle_{r,\vartheta,z}}$

$$\begin{aligned} Re_i(t) &= \frac{U_0 H}{\nu} \sqrt{\left\langle u_i^2(t) \right\rangle_{r,\vartheta,z}} : \; i = \{r, \vartheta, z\} \\ &= \sqrt{\frac{Ra}{Pr}} \sqrt{\left\langle u_i^2(t) \right\rangle_{r,\vartheta,z}}. \end{aligned} \tag{2.6}$$

These Reynolds numbers allow the distinction of the strength of fluid motion in the different directions, i.e. radial, azimuthal and vertical directions. Consequently, their ratios can depict the predominant flow motion and will help to classify characteristic

flow states. Temporal averaging starts when the statistically stationary state has been reached.

The ratio of thermal to kinetic boundary layer thicknesses plays a crucial role in Ekman pumping related heat transport enhancement (Stevens *et al.* 2010*b*; Yang *et al.* 2020). We determine the thermal boundary layer thickness λ_Θ from the vertical profile of the horizontally averaged temperature (e.g. Stevens *et al.* 2010*a*), where λ_Θ is defined as the intersection between the temperature gradient at the plate with a linear fit to the temperature profile in the bulk ($0.2 \leqslant z \leqslant 0.8$). Following Stevens *et al.* (2010*a*) and Yang *et al.* (2020), the kinetic boundary layer thickness λ_u is estimated as twice the height of the peak location of the horizontally averaged quantity $\langle \boldsymbol{u} \cdot \nabla^2 \boldsymbol{u} \rangle_H$. The horizontal averages involve only 90 % of the radial distance from the axis, which in our case worked best to consistently exclude effects of the sidewall boundary layer (Wagner, Shishkina & Wagner 2012). The reported values are averaged over top and bottom boundary layers.

3. Heat transport maxima under rotation and confinement

First, we keep $Ra = 7 \times 10^8$ (and $Pr = 4.38$) fixed and vary the confinement parameter Γ^{-1} and the rotation rate Ro^{-1}. When, on the one hand, Γ^{-1} is varied in the absence of rotation $Ro^{-1} = 0$, the normalized heat transport Nu/Nu_0 is largest for $\Gamma^{-1} = 12$ (figure 1*a*). When, on the other hand, Ro^{-1} is varied in a relatively wide cylinder with $\Gamma^{-1} = 3$, the largest Nu/Nu_0 is reached at $Ro^{-1} \approx 8$. Both are known as the heat transport enhancement by either moderate confinement (e.g. Huang *et al.* 2013; Chong *et al.* 2015) or moderate rotation (e.g. Zhong *et al.* 2009; Kunnen *et al.* 2011). However, surprisingly, the two-dimensional parameter subspace of Γ^{-1} and Ro^{-1} reveals a strongly non-symmetric enhancement of the heat transport when both confinement and rotation are present simultaneously (figure 1*a*). Hence, the enhancing effects of both types of stabilization do not simply superpose with each other. Instead they interact in a more complex way.

Our simulations reveal three separate maxima of the heat transport (figure 1*a*). Maximum A is the heat transport enhancement by moderate confinement in the absence of rotation, which vanishes already under weak rotation. Therefore, we will hereafter refer to it as the *confinement* maximum. On the contrary, the enhancement by moderate rotation Ro^{-1} in large domains does not directly vanish with increasing confinement Γ^{-1} (figure 1*a*). It further extends into the (Ro^{-1}, Γ^{-1}) parameter space and even increases up to maximum B, which is the largest heat transport achieved for $Ra = 7 \times 10^8$. Thereby, the range of Ro^{-1}, which enhances the heat transport, shifts towards faster rotation with increasing Γ^{-1}, and separates from the *confinement* maximum. The onset of heat transport enhancement strongly correlates with $Re_z = Re_H = (Re_\vartheta^2 + Re_r^2)^{1/2}$, the transition from buoyancy-dominated to rotation-controlled regime (figure 1*b*; thick grey line), which will be further discussed in § 4. Even more surprisingly, we observe a third maximum C at the tip of the enhancement region around maximum B.

All maxima are associated with an individual (sub-)regime of the fluid motion (figure 1*b*), which characterizes the flow pattern around each maximum. At the *confinement* maximum the flow forms vertically coherent buoyant plumes (figure 2*a*). At maximum B the flow is organized in two stable vortices (figure 3*a*). Hence, we will hereafter refer to it as the *double-vortex* maximum. At maximum C the flow is characterized by one stable central vortex (figure 4*a*). Accordingly, we will refer to it as

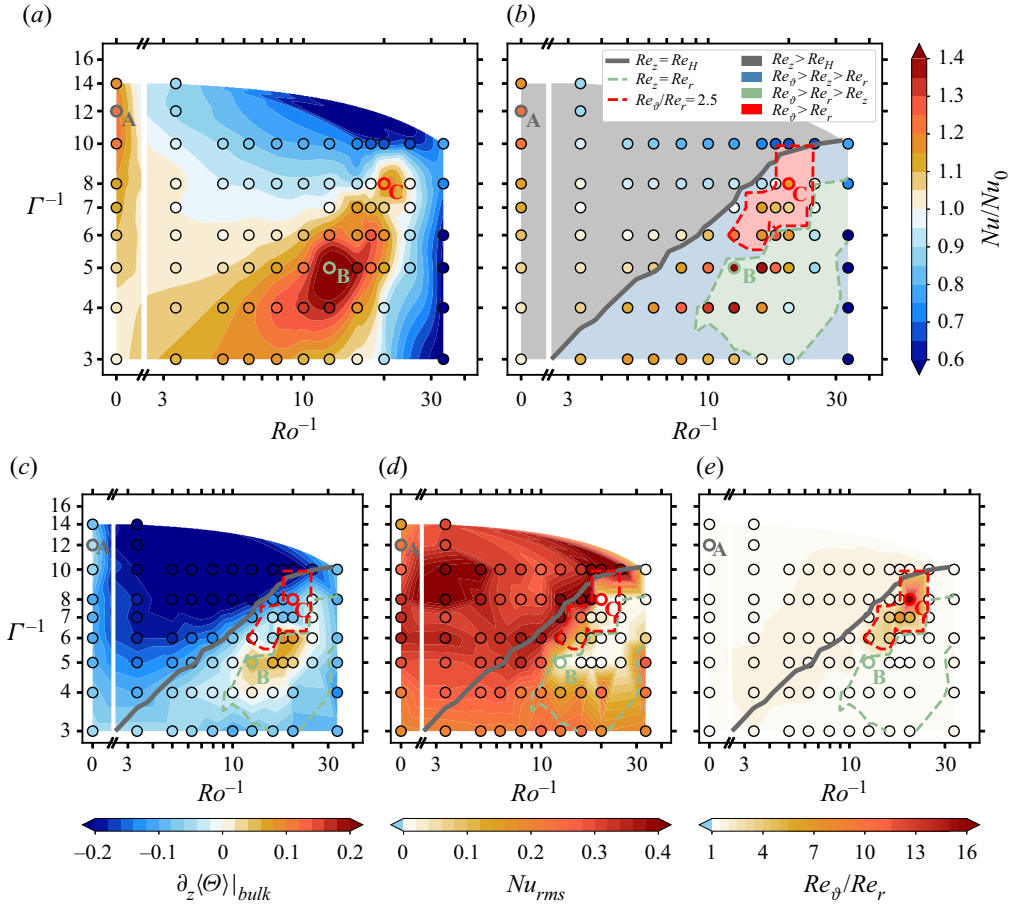

Figure 1. Heat transport maxima and flow characteristics in the parameter space of rotation Ro^{-1} and confinement Γ^{-1} for $Ra = 7 \times 10^8$. A, B and C mark the positions of the *confinement* (§ 3.1), *double-vortex* (§ 3.2) and *single-vortex* maxima (§ 3.3), respectively. Grey, green and red lines show the transitions between the (sub-)regimes of prominent flow characteristics. (*a*) Normalized heat transport Nu/Nu_0 (circles, data points; background, cubic interpolation). (*b*) Regimes of prominent flow motion based on linear interpolation of $Re_{\vartheta,r,z}$ data. The grey area depicts the buoyancy-dominated regime ($Re_z > Re_H = (Re_\vartheta^2 + Re_r^2)^{1/2}$). The coloured areas belong to the rotation-controlled regime ($Re_H > Re_z$). In the green sub-regime the characteristic flow motion ($Re_\vartheta > Re_r > Re_z$) indicates *double-vortex* flow. In the red sub-regime suppressed radial motion (see (*e*)) indicates *single-vortex* flow. The symbol colour shows again the heat transport Nu/Nu_0. (*c*) Mean vertical temperature gradient in the bulk $\langle\partial_z\langle\Theta\rangle_{r,\vartheta,t}\rangle_{0.2\leqslant z\leqslant 0.8}$ (circles, data points; background, linear interpolation). (*d*) Temporal stability of the flow based on Nu_{rms} ((2.5), circles, data points; background, linear interpolation). (*e*) Ratio of azimuthal to radial Reynolds numbers Re_ϑ/Re_r (circles, data points; background, linear interpolation).

the *single-vortex* maximum. Next, we present each of the three maxima and its specific flow dynamics separately in detail (§§ 3.1–3.3).

3.1. *Flow organization around the* confinement *maximum (A)*

At the *confinement* maximum, the flow tends to organize into two plumes: one up- and one downwelling plume of hot and cold fluid, respectively (figure 2*a*). Both plumes

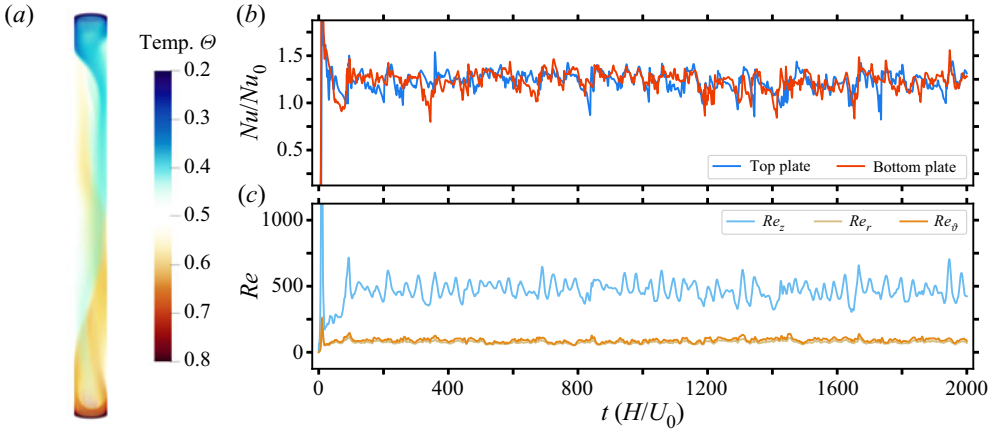

Figure 2. Flow characteristics at the *confinement* maximum at $Ra = 7 \times 10^8$ ($\Gamma^{-1} = 12$, $Ro^{-1} = 0$): (*a*) snapshot of the temperature field, (*b*) temporal evolution of $Nu(t)$ at the top and bottom plate, (*c*) temporal evolution of $Re(t)$ for each velocity component.

span the entire vertical distance and connect the boundary layers along top and bottom plates (Hartmann *et al.* 2021). Both plumes are entangled such that they emerge around the sidewalls and impact at the centre on the opposite plate. At boundary layer height this structure yields the same characteristic pattern of plume distribution for the optimal heat transport in confined RBC (Chong *et al.* 2015, 2017). The integral quantities Nu and Re (figure 2*b*,*c*) are strongly fluctuating in time, which indicates that – typical for turbulent convection – these plumes are relatively unstable. Vertical motion is predominant ($Re_z \gg Re_{\vartheta,r}$, figure 2*c*) as expected in the buoyancy-dominated regime in which $Re_z > Re_H = (Re_\vartheta^2 + Re_r^2)^{1/2}$ (figure 1*b*; grey area).

Further, the *confinement* maximum in a cylindrical domain correlates with a local minimum of the temperature gradient in the bulk (figure 1*c*, see also Hartmann *et al.* 2021). A flatter bulk gradient can indicate two situations: more turbulent mixing in general, or larger mutual vertically coherent structures that compensate each other in the horizontal average within the entire bulk region. Obviously, the second is the case at the *confinement* maximum. At the optimal confinement, a domain-spanning *double-plume* structure is triggered, which maximizes this effect. Moderate confinement reduces horizontal mixing and thereby supports vertical transport and the formation of vertically coherent structures (Chong *et al.* 2015; Chong & Xia 2016; Chong *et al.* 2017). When Γ^{-1} is increased beyond the optimum, the growing impact of the sidewalls reduces the heat transport (Chong *et al.* 2015; Chong & Xia 2016). Similarly, coherent flow structures in wall-normal direction help to maximize the heat transport in inclined-confined RBC (Zwirner & Shishkina 2018).

3.2. *Flow organization around the* double-vortex *maximum (B)*

At the *double-vortex* maximum, the flow consists of two vortices, one vortex of hot (cold) fluid that emerges from the bottom (top) plate (figure 3*a*). Both span the entire domain side by side and connect top and bottom boundary layers. Such vertically aligned vortices are typically observed at the heat transport maximum in the rotation-controlled regime (e.g. Stevens, Clercx & Lohse 2012). This flow structure appears to be very steady after it has fully developed for $Ra = 7 \times 10^8$ (figure 3*b*,*c*). The *double-vortex* structure

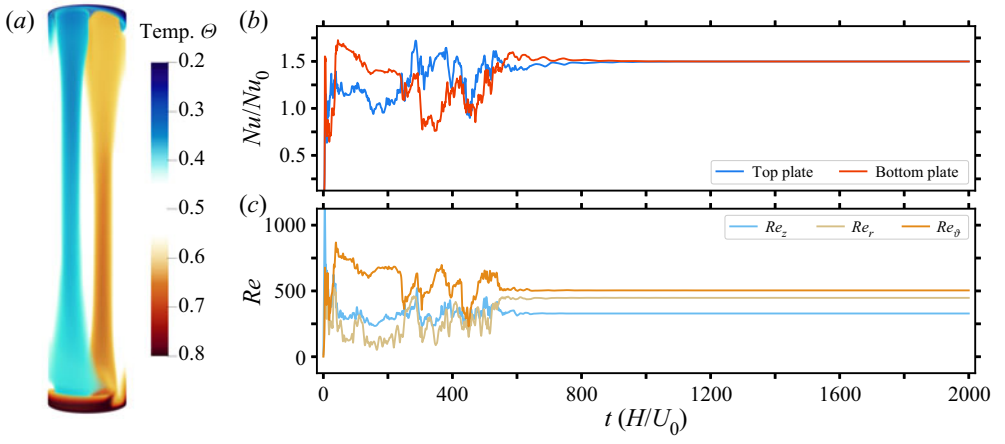

Figure 3. Flow characteristics at the steady *double-vortex* maximum at $Ra = 7 \times 10^8$ ($\Gamma^{-1} = 5, Ro^{-1} = 12.5$): (*a*) snapshot of the temperature field, (*b*) temporal evolution of $Nu(t)$ at the top and bottom plate, (*c*) temporal evolution of $Re(t)$ for each velocity component.

is characterized by a different configuration of mean fluid motion in the flow: both lateral motions, azimuthal Re_ϑ and radial Re_r, are significantly larger than the vertical motion Re_z (figure 3*c*). In particular, we observe $Re_\vartheta > Re_r > Re_z$, which will serve as an indicator to identify the formation of *double-vortex* flow (figure 1*b*). The temporal stability of this flow structure is also visible in the Nusselt number fluctuations Nu_{rms} (2.5). We find a region with stable flow formation in the (Ro^{-1}, Γ^{-1}) parameter space around the *double-vortex* and the *single-vortex* maxima (figure 1*d*). The appearance of stable flow co-occurring with enormous heat transport enhancement in the sub-regime of *double-vortex* flow can be linked to a stabilizing temperature gradient in the bulk $\langle \partial_z \langle \Theta \rangle_{r,\vartheta,t} \rangle_{0.2 \leqslant z \leqslant 0.8} > 0$ (figure 1*c*). Such a temperature inversion is known to stabilize flow formations (Tilgner, Belmonte & Libchaber 1993; Brown & Ahlers 2007), in this case the two opposing domain-spanning Ekman vortices. Consequently, cylindrical confinement plays a crucial role in maximizing the heat transport by stabilizing the *double-vortex* state in a very narrow range of (Ro^{-1}, Γ^{-1}) combinations.

3.3. *Flow organization around the* single-vortex *maximum (C)*

At the *single-vortex* maximum, the flow organizes itself in one central vortex of cold (or hot) fluid sinking (rising) from the top (bottom) plate and a curtain of hot (cold) fluid rising (sinking) at the sidewall (figure 4*a*). At the maximum this *single-vortex* flow is also very stable (figure 4*b*,*c*), although it is not top–bottom symmetric. Also, the *single-vortex* maximum is related to a very distinct flow organization (figure 4*c*). Again, azimuthal motion Re_ϑ is predominant, and thus horizontal motion Re_H is also stronger than vertical motion Re_z. However, radial motion Re_r is almost entirely suppressed in the *single-vortex* state. This results in an extreme ratio between the lateral components $Re_\vartheta / Re_r \gg 1$, a geometric effect of a singular vortex centred in a cylindrical coordinate system. In this case, the vortex itself does not have a radial flow component. Radial motion occurs only close to the top and bottom plates. On the contrary, any off-centred vortex contains a radial flow component in the cylindrical reference system.

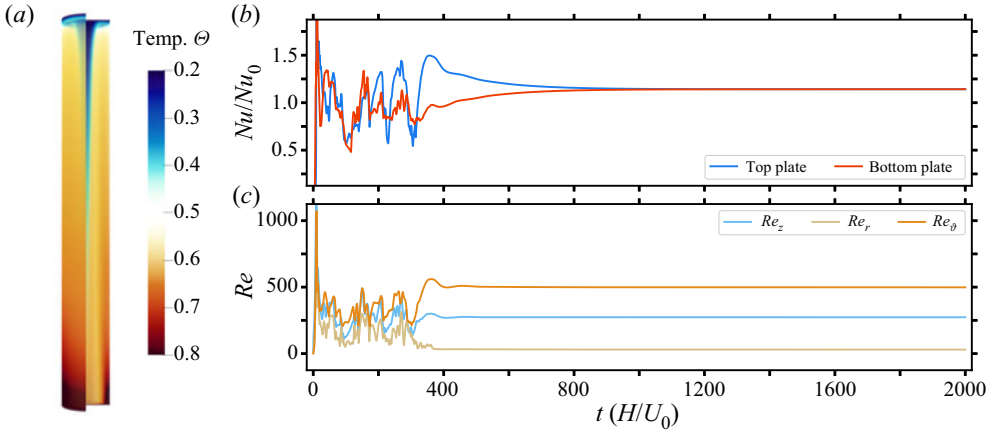

Figure 4. Flow characteristics at the steady *single-vortex* maximum at $Ra = 7 \times 10^8$ ($\Gamma^{-1} = 8$, $Ro^{-1} = 20$): (*a*) snapshot of the temperature field, (*b*) temporal evolution of $Nu(t)$ at the top and bottom plate, (*c*) temporal evolution of $Re(t)$ for each velocity component.

Nevertheless, the presence of a *single-vortex* flow structure in the (Ro^{-1}, Γ^{-1}) parameter space can be identified by a significantly increased ratio $Re_\vartheta/Re_r \gg 1$ with its maximum directly located at the *single-vortex* heat transport maximum (figure 1*e*). The other maxima do not show any significant dependence on this ratio (elsewhere $Re_\vartheta/Re_r \approx 1$). *Single-vortex* flow is limited to a small regime in the (Ro^{-1}, Γ^{-1}) parameter space and the transition is very sharp. Only between the *single-vortex* maximum and the *double-vortex* maximum can a more gradual increase of the ratio Re_ϑ/Re_r be identified (figure 1*e*). For our data, an arbitrary threshold of $Re_\vartheta/Re_r \geqslant 2.5$ is appropriate to identify the sub-regime of *single-vortex* flow (figure 1*e*,*b*). The existence of *single-vortex* flow (figure 1*e*) corresponds well with the partial region of steady flow formation (figure 1*d*) that has not been linked to bulk temperature inversion due to *double-vortex* flow (figure 1*c*).

Single-vortex flow is always related to an extreme ratio Re_ϑ/Re_r, but it can be interrupted by periods of turbulent mixing for (Ro^{-1}, Γ^{-1}) combinations beside the maximum (Appendix B: figure 11). We assume that the *single-vortex* flow in one configuration becomes unstable due to its lack of symmetry and recovers it by reverting the flow configuration. Interestingly, the temporal stability of *single-vortex* flow increases (periods of steady *single-vortex* flow elongate) towards the maximum where no instability has been observed (figure 4*b*,*c*). Thus, the time-averaged Re_ϑ/Re_r ratio does also reflect the temporal stability of the *single-vortex* flow (figure 1*e*). Whether the flow can be infinitely stable in one configuration at the *single-vortex* maximum remains an open question.

We note that, although the sidewall obviously plays an essential role for *single-vortex* flow, the flow dynamics is very different from the recently observed boundary zonal flow (Zhang *et al.* 2020). First, in *single-vortex* flow, either hot or cold fluid is transported along the sidewall, while in boundary zonal flow both hot and cold plumes alternate. Second, *single-vortex* flow includes a convective bulk, whereas for boundary zonal flow the bulk is at rest. Third, *single-vortex* flow is steady, whereas boundary zonal flow is still turbulent. Finally, the two are observed in different parameter ranges, suggesting that both are only local – not global – states in the parameter space.

4. Interfering effects for heat transport enhancement

The central mechanism for heat transport enhancement under rotation is Ekman pumping (e.g. Rossby 1969). The common view is that the onset of Ekman pumping causes the transition from a large-scale circulation to vertically aligned vortices, which can result in heat transport enhancement (Julien *et al.* 1996). Although it has been recently observed that the onset of heat transport enhancement and the change in flow dynamics have slightly different onsets (Alards *et al.* 2019), both are certainly closely related to each other.

In this work, we define the transition from buoyancy-dominated to rotation-controlled regime by the change of the predominant fluid motion from vertical to horizontal, i.e. at $Re_z = Re_H$ (figure 1*b*; thick grey line). The transition $Re_z = Re_H = (Re_\vartheta^2 + Re_r^2)^{1/2}$ describes the onset of heat transport enhancement in very confined systems significantly better than the commonly used transition of the kinetic boundary layer from Prandtl–Blasius type to Ekman type (Appendix B: figure 12). We note that, in this context, any Ekman pumping related increase of Nu with Ro^{-1} is seen as heat transport enhancement independent of whether $Nu/Nu_0 > 1$ or not. In our view, it is reasonable that vertical motion is predominant in the buoyancy-dominated regime, and horizontal motion takes over in the rotation-controlled regime, when vortical structures dominate the flow. The vortical structures extend the vertical transport induced by Ekman pumping through the bulk, which thereby increases the heat transport. We observe that all simulations with a rotation enhanced heat transport are characterized by $Re_H > Re_z$, and that the onset is located just beyond this transition (figure 1*b*).

Both the transition $Re_z = Re_H$ and the onset of heat transport enhancement simultaneously shift towards faster rotation Ro^{-1} with increasing confinement Γ^{-1}. With increasing Γ^{-1}, the cylinder diameter approaches the critical length scale of convective instability $L_c = 4.82 \times Ek^{1/3}$ for rotating RBC (Chandrasekhar 1961; Kunnen *et al.* 2016). We assume that the formation of vortical flow structures requires a minimal lateral size, i.e. a maximal confinement $\Gamma_{max}^{-1}(L_c)$, which can be reached with faster rotation. Consequently, the transitional rotation rate $Ro_{BD\text{-}RC}^{-1}$ for the onset of heat transport enhancement is strongly Γ^{-1}-dependent in slender cylinders, but might be insensitive to Γ^{-1} in sufficiently wide domains. Several approaches employ a Ginzburg–Landau model to account for the Γ^{-1}-dependence (e.g. Weiss *et al.* 2010; Weiss & Ahlers 2011*b*), but ignore any Ra-dependence, which will be addressed in § 5.

Ideally, an equal thickness of thermal and kinetic boundary layer is supposed to maximize the heat transport in rotating RBC (e.g. Julien *et al.* 1996; King *et al.* 2009), since Ekman pumping becomes most efficient in ejecting heat from the boundary layers into the columnar vortices (Stevens *et al.* 2010*b*). However, this is only valid up to a certain Ra and confinement (Yang *et al.* 2020). Similar to Yang *et al.* (2020), we test this assumption by mapping the heat transport onto the ratio of thermal and kinetic boundary layer thicknesses λ_Θ/λ_u for fixed confinement Γ^{-1} (figure 5). Thereby, an increasing λ_Θ/λ_u is generally related to an increasing Ro^{-1}. Accordingly, our widest cylinder ($\Gamma^{-1} = 3$) shows a relatively symmetric heat transport enhancement around $\lambda_\Theta/\lambda_u = 1$ (figure 5*a*). With increasing confinement ($\Gamma^{-1} = 4$), the maximal heat transport at $\lambda_\Theta/\lambda_u \approx 1$ significantly increases but also gains some asymmetry around the enhancement peak (figure 5*a*). Thereby, the large heat transport coincides with the presence of *double-vortex* flow (figure 5*d*; green symbols). For confinement $\Gamma_{2VM}^{-1} = 5$, at which the *double-vortex* maximum is obtained, the peak is still located close to $\lambda_\Theta/\lambda_u = 1$, but with a rather sharp onset just at $\lambda_\Theta/\lambda_u \approx 1$ (figure 5*b*). The largest heat transport is again associated with stable *double-vortex* flow (figure 5*e*; green symbols). In slender

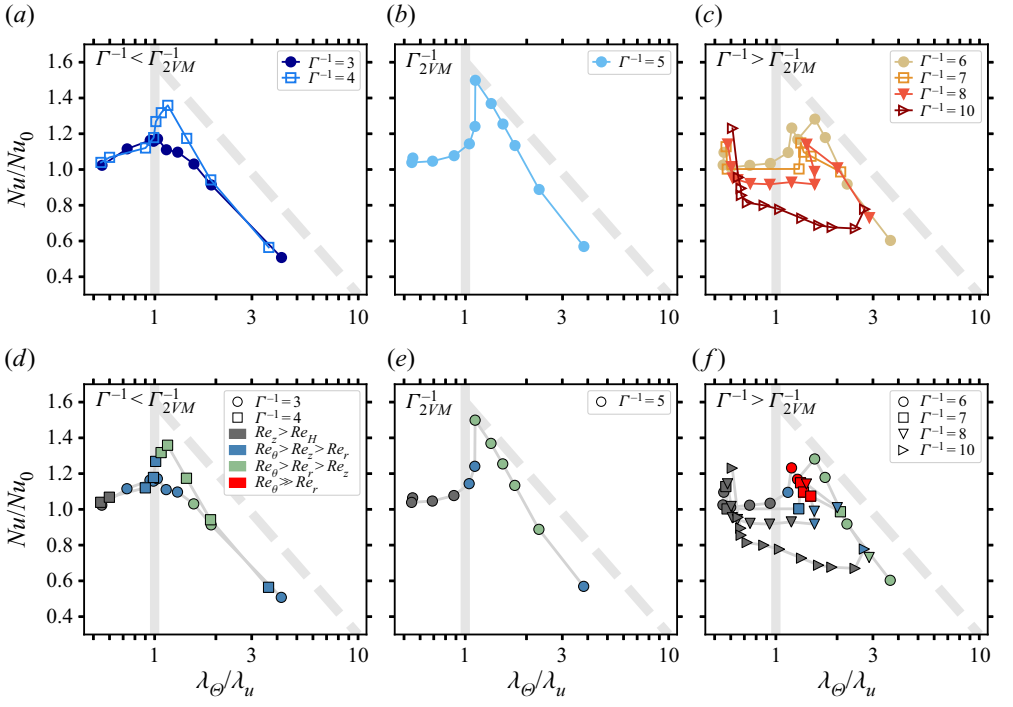

Figure 5. Normalized heat transport Nu/Nu_0 mapped onto the ratio of thermal and kinetic boundary layers λ_Θ/λ_u for various Γ^{-1} at $Ra = 7 \times 10^8$: (*b*) for $\Gamma^{-1}_{2VM} = 5$, where the *double-vortex* maximum is observed, (*a*) for less confinement $\Gamma^{-1} < \Gamma^{-1}_{2VM}$, i.e. wider cylinders than in (*b*), (*c*) for more confinement $\Gamma^{-1} > \Gamma^{-1}_{2VM}$, i.e. more slender cylinders than in (*b*). (*d–f*) Same data as in (*a–c*), respectively, but symbols coloured in their corresponding regime of prominent flow motion (figure 1*b*): grey – buoyancy-dominated regime, blue – rotation-controlled regime, green – rotation-controlled with *double-vortex* flow (figure 3*a*), red – rotation-controlled with *single-vortex* flow (figure 4*a*). The vertical grey line marks the most beneficial boundary layer ratio $\lambda_\Theta/\lambda_u = 1$. The dashed grey line (no specific scaling) serves as guide for the eye. The coloured and grey lines connecting the data points in (*a–c*) and (*d–f*), respectively, follow increasing rotation Ro^{-1} per confinement Γ^{-1}.

cylinders ($\Gamma^{-1} > \Gamma^{-1}_{2VM}$), no enhancement can be observed around $\lambda_\Theta/\lambda_u = 1$ (figure 5*c*). Still, large heat transport is observed twice: (i) rotation induced enhancement only appears at $\lambda_\Theta/\lambda_u > 1$ again with an extremely sharp onset. The largest heat transport again coincides with *double-vortex* or *single-vortex* flow (figure 5*f*; green and red symbols). (ii) Large heat transport at $\lambda_\Theta/\lambda_u \approx 0.6 < 1$ corresponds to the non-rotating cases and the enhancement due to confinement (§ 3.1), which is different from the expectation $\lambda_\Theta/\lambda_u \approx 1$ based on the unifying view of Chong *et al.* (2017). We explain this deviation by the different definitions used to determine the kinetic boundary layer thickness. This, however, seems to affect mainly the estimates for the non-rotating confined cases. Nonetheless, the kinetic and thermal boundary layers themselves evolve in general as expected (see Appendix B: figures 12*b*, 13).

The sharp onsets for $\Gamma^{-1} \geqslant \Gamma^{-1}_{2VM}$ result from a shifted transition from the buoyancy-dominated to the rotation-controlled regime. In less confined domains ($\Gamma^{-1} < \Gamma^{-1}_{2VM}$), the rotation-controlled regime already begins at $\lambda_\Theta/\lambda_u \ll 1$ and thus the efficiency of Ekman pumping can symmetrically increase and decrease around $\lambda_\Theta/\lambda_u = 1$ (figure 5*d*; blue symbols). However, as long as the flow is buoyancy-dominated, no

vortical structure can profit from Ekman pumping to enhance the heat transport, even for a beneficial ratio $\lambda_\Theta/\lambda_u \approx 1$ (figure 5*e*,*f*; grey symbols). When the rotation-controlled regime begins at $\lambda_\Theta/\lambda_u \geqslant 1$, Ekman pumping is immediately most effective, resulting in a sharp increase of the heat transport, which afterwards decreases again with further increase of λ_Θ/λ_u (figure 5*b*,*c*). Heat transport enhancement does still exist even when the rotation-controlled regime begins at $\lambda_\Theta/\lambda_u \gg 1$, but may not suffice to exceed the reference heat transport Nu_0 (figure 5*c*,*f*; $\Gamma^{-1} = 10$). These observations show that Ekman pumping is the essentially required mechanism for heat transport enhancement, and that the combination with a boundary layer ratio $\lambda_\Theta/\lambda_u \approx 1$ is the beneficial condition.

Ekman pumping is always present in all rotating (sub-)regimes (figure 1*b*; blue, green, red areas). However, its net contribution to heat transport enhancement depends on the boundary layer ratio $\lambda_\Theta/\lambda_u \approx 1$, which determines the efficiency of heat injection into the Ekman vortices (Stevens *et al.* 2010*b*). With increasing rotation vertical (heat) transport is suppressed, which leads to a thicker thermal boundary layer and hence a larger ratio λ_Θ/λ_u. Accordingly, the envelope of the normalized heat transport among all Γ^{-1} decreases with increasing boundary layer ratio for $\lambda_\Theta/\lambda_u > 1$ (figure 5). Another way to grasp this limiting effect is the intrinsic relation of Nu/Nu_0 and λ_Θ/λ_u via the thermal shortcut. However, for the same boundary layer ratio λ_Θ/λ_u, i.e. for the same efficiency for heat being injected into the Ekman vortices, the heat transport is mostly largest whenever a stable, domain-spanning flow structure (*single vortex* or *double vortex*) is formed (figure 5*d–f*; green and red vs blue symbols). Moreover, *single-vortex* flow is less efficient than *double-vortex* flow for $Ra = 7 \times 10^8$ (figure 5*e*,*f*; green vs red symbols). Taken together, the heat transport with *double-vortex* or *single-vortex* flow clusters above the heat transport without a specific vortex structure, but within all regimes the heat transport decreases with increasing $\lambda_\Theta/\lambda_u > 1$. This nicely depicts the superposing impacts of the boundary layer ratio and a stable, domain-spanning flow formation (figure 5*d–f*).

In summary, we identified two effects that affect the efficiency of Ekman pumping in the rotation-controlled regime. Both effects can be characterized differently. First, the boundary layer ratio λ_Θ/λ_u determines how effective heat is injected from the boundary layer *into* the bulk. Therefore, we refer to it as a heat injection effect. Second, certain combinations of confinement Γ^{-1} and rotation Ro^{-1} lead to stable and vertically domain-spanning flow structures, which increase the efficiency of heat transported *through* the bulk. It is, therefore, a bulk transport effect. Several sub-regimes of stable, domain-spanning flow, which interfere with the effectiveness of the boundary layer ratio, result in the multiple maxima of heat transport under rotation and confinement.

5. Dependence on the Rayleigh number

We will now demonstrate how the three heat transport maxima (§ 3) depend on Ra. Therefore, we explore the (Ro^{-1}, Γ^{-1}) parameter space at four values of $Ra = 2 \times 10^8$, 7×10^8, 2.3×10^9 and 7×10^9 (figure 6). For each Ra we can identify the different regimes of flow motion with their associated heat transport maxima (*confinement*, *double vortex* and *single vortex*). The *confinement* maximum is clearly present for all Ra, and always disappears when rotation is added (figure 6). The magnitude of heat transport enhancement increases with increasing Ra (figure 7*a*), and shifts towards stronger confinement (figure 7*c*) as also observed by Chong *et al.* (2015) and Hartmann *et al.* (2021).

The *double-vortex* maximum is present at all four Ra, but with a sharp drop of its enhancement efficiency between $Ra = 7 \times 10^8$ and $Ra = 2.3 \times 10^9$. For the lower

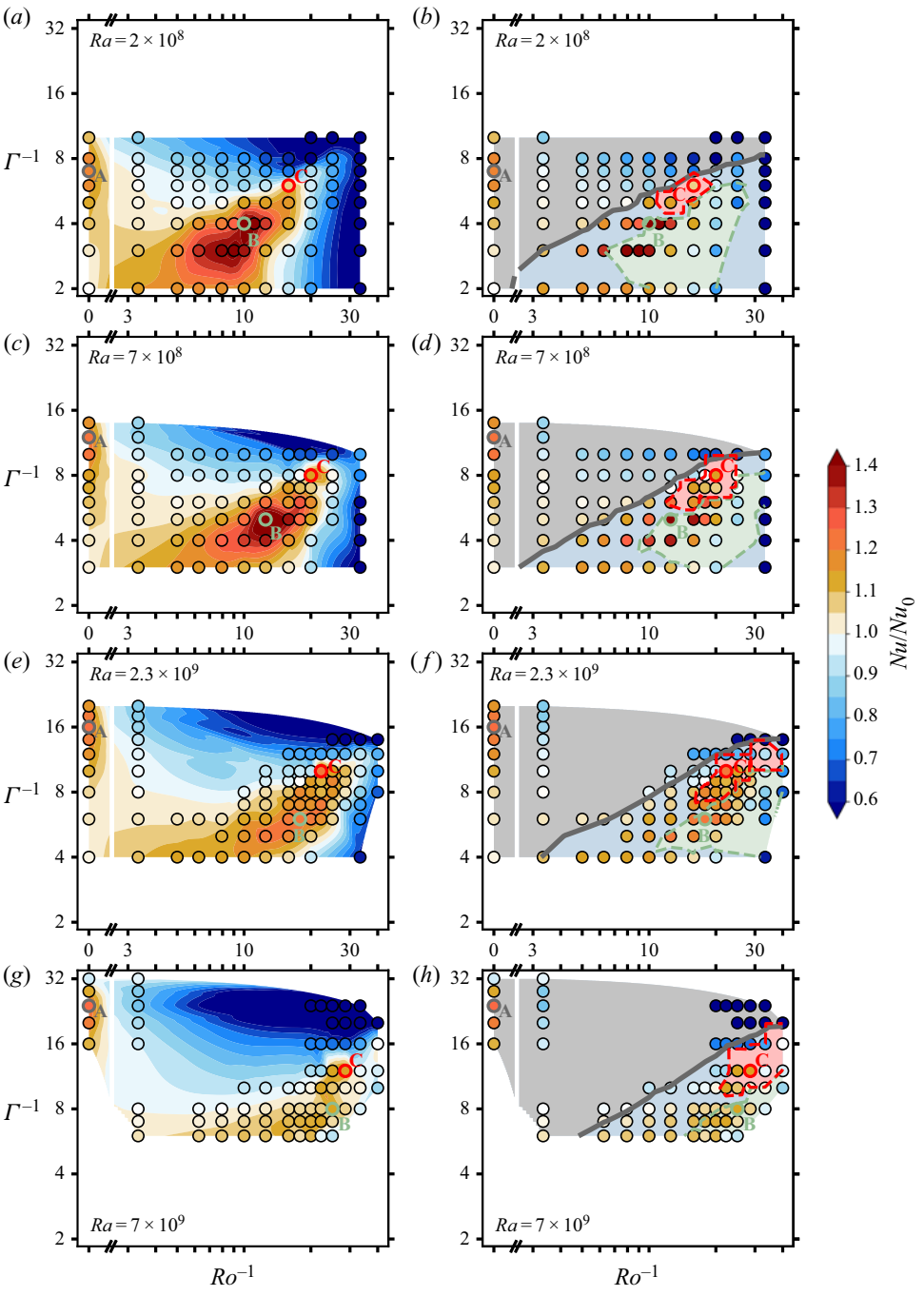

Figure 6. Heat transport (a,c,e,g) and regimes of prominent flow motion (b,d,f,h) in the parameter space of rotation rate Ro^{-1} and cylinder confinement Γ^{-1} at four Ra. A, B and C mark the position of the *confinement* (§ 3.1), *double-vortex* (§ 3.2) and *single-vortex* maxima (§ 3.3), respectively. Grey, green and red lines show the transitions between the (sub-)regimes of prominent flow motion. The grey area depicts the buoyancy-dominated regime ($Re_z > Re_H$). The coloured areas belong to the rotation-controlled regime ($Re_H > Re_z$). In the green and red sub-regimes the characteristic flow motion indicates the *double-vortex* and *single-vortex* flow, respectively. The symbol colour always shows the heat transport Nu/Nu_0. Nu_0 is the heat transport of the non-rotating $\Gamma^{-1} = 1$ case at each Ra. See also figure 1(a,b) for detailed description.

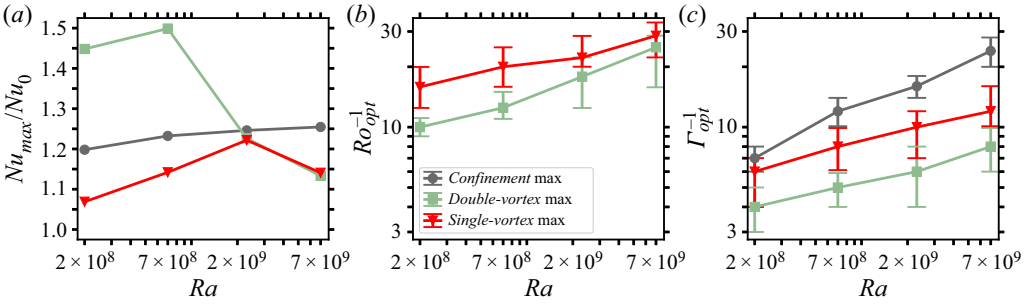

Figure 7. (*a*) Normalized heat transport Nu_{max}/Nu_0 of the three maxima as a function of Ra. Here, Nu_0 is the heat transport of the non-rotating $\Gamma^{-1} = 1$ case at each Ra. (*b*) Rotation rate Ro^{-1}_{opt} of the *double-vortex* and *single-vortex* maxima as a function of Ra. (*c*) Confinement parameter Γ^{-1}_{opt} of the three maxima as a function of Ra.

$Ra = 2 \times 10^8, 7 \times 10^8$, the *double-vortex* maximum achieves the largest enhancements within this study by up to 50 %, whereas the enhancement drops to less than 20 % for larger $Ra = 2.3 \times 10^9, 7 \times 10^9$, which is even below the heat transport of the *confinement* maximum that then becomes the most efficient (figure 7*a*). Although the magnitude of heat transport enhancement decreases, the region of enhanced heat transport around the *double-vortex* maximum (where $Nu > Nu_0$) enlarges significantly with increasing Ra. Most prominently the enhancement region enlarges towards larger Ro^{-1} and Γ^{-1}, concurrent with the shift of the associated flow regimes (figure 6). This entire behaviour of the heat transport enhancement can be explained by an interference of the two enhancing effects, beneficial boundary layer ratio and stable vortex formation.

To illustrate this interference that explains the above behaviour (figures 6, 7*a*), we show again the heat transport mapped onto the boundary layer ratio (as in figure 5), but now for selected confinement parameters Γ^{-1} among all four Ra values (figure 8). Note that, in this plot, we assign each combination of Γ^{-1} and Ra relative to its associated optimal confinement of the *double-vortex* maximum $\Gamma^{-1}_{2VM}(Ra)$, i.e. $\Gamma^{-1} = 6 > \Gamma^{-1}_{2VM}(Ra = 2 \times 10^8) = 4$ (figure 8*c*), but $\Gamma^{-1} = 6 < \Gamma^{-1}_{2VM}(7 \times 10^9) = 8$ (figure 8*a*). The strong enhancement at lower Ra results from the coincidence that, around the most beneficial boundary layer ratio $\lambda_\Theta/\lambda_u \approx 1$, the flow (i) experiences Ekman pumping, and (ii) forms a stable *double-vortex* structure (figures 8*b*,*e* and 8*a*,*d*). Consequently, both enhancing effects interfere most efficiently, but also most locally around $\lambda_\Theta/\lambda_u = 1$ and in the (Ro^{-1}, Γ^{-1}) parameter space. On the other hand, at larger Ra, the rotation-controlled regime begins only at $\lambda_\Theta/\lambda_u \gtrsim 1$, which already reduces the largest achievable efficiency of Ekman pumping. Moreover, *double-vortex* flow is only formed at larger λ_Θ/λ_u, and thus it co-occurs only with a weak efficiency from the boundary layer ratio. Hence, the *double-vortex* maximum forms, where the interference of both effects is still the largest, but not as ideal as at lower Ra. As a consequence, *double-vortex* flow at its maximum is less stable at larger Ra than at lower Ra (figure 9). Still, whenever *double-vortex* flow can be identified, the heat transport is temporary strongly enhanced (figure 9; shaded areas). In brief, the shift of the *double-vortex* flow regime away from $\lambda_\Theta/\lambda_u \approx 1$ for larger Ra reduces the interference of the two enhancing effects, and therefore enlarges the region of heat transport enhancement while flattening the *double-vortex* maximum.

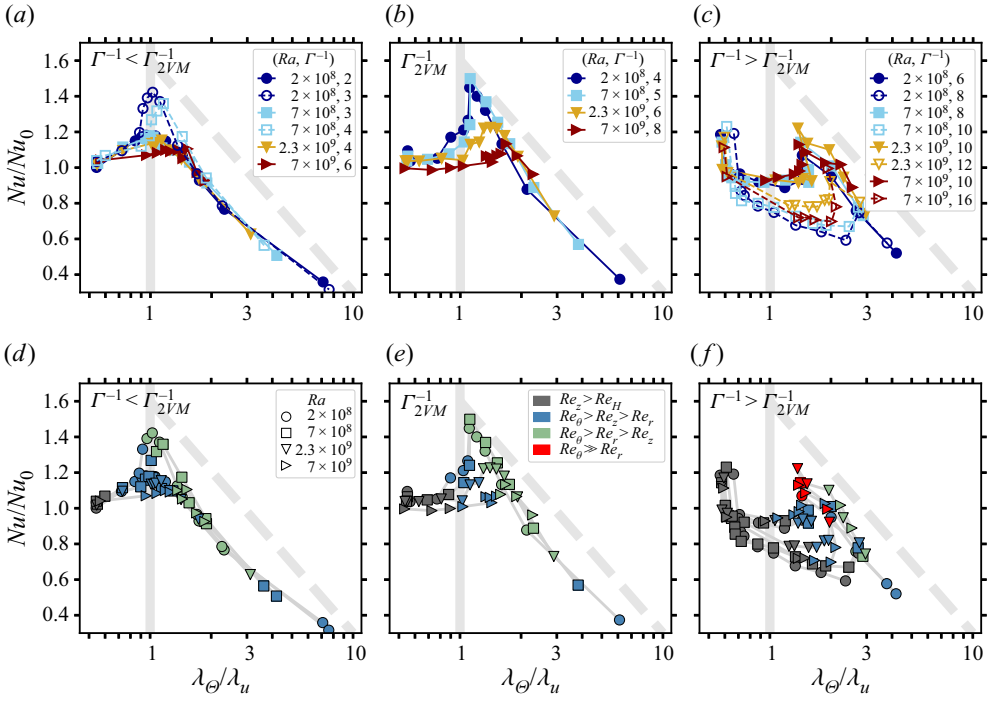

Figure 8. Normalized heat transport Nu/Nu_0 mapped onto the ratio of thermal and kinetic boundary layers λ_Θ/λ_u for various combinations of Γ^{-1} and Ra: (*b*) for $\Gamma^{-1}_{2VM}(Ra)$, where the *double-vortex* maximum is observed at each value of Ra, (*a*) for less confinement $\Gamma^{-1} < \Gamma^{-1}_{2VM}(Ra)$, i.e. wider cylinders than in (*b*), (*c*) for more confinement $\Gamma^{-1} > \Gamma^{-1}_{2VM}(Ra)$, i.e. more slender cylinders than in (*b*). (*d–f*) Same data as in (*a–c*), respectively, but symbols coloured in their corresponding regime of prominent flow motion (figure 6): grey – buoyancy-dominated regime, blue – rotation-controlled regime, green – rotation-controlled with *double-vortex* flow, red – rotation-controlled with *single-vortex* flow. The vertical grey line marks the most beneficial boundary layer ratio $\lambda_\Theta/\lambda_u = 1$. The dashed grey line (no specific scaling) serves as guide for the eye. The coloured and grey lines connecting the data points in (*a–c*) and (*d–f*), respectively, follow increasing rotation Ro^{-1} per confinement Γ^{-1}.

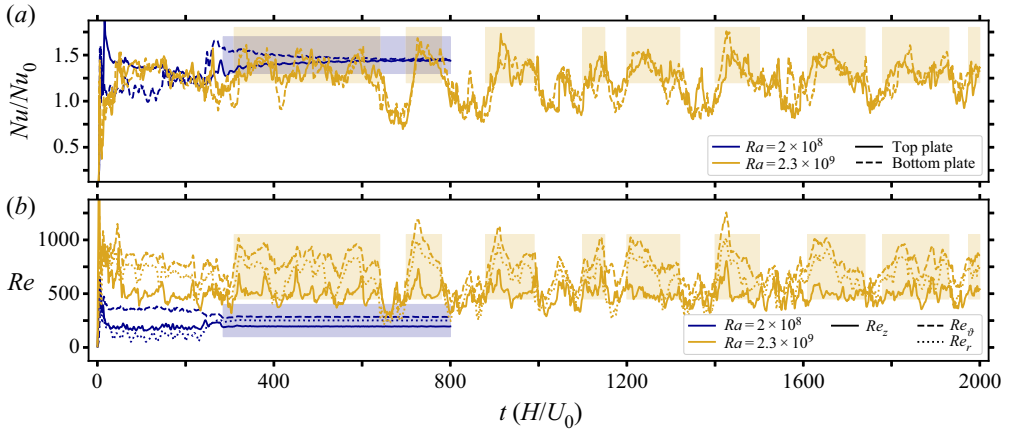

Figure 9. Flow characteristics at the *double-vortex* maximum at $Ra = 2 \times 10^8$ and $Ra = 2.3 \times 10^9$: (*a*) temporal evolution of $Nu(t)$ at the top and bottom plates, (*b*) temporal evolution of $Re(t)$ for each velocity component. The shaded areas indicate when *double-vortex* flow (as in figure 3*a*) is observed.

For very large Ra, this shift could result in a segregation of the *double-vortex* maximum into two separate maxima, one originating from the most effective boundary layer ratio $\lambda_\Theta/\lambda_u \approx 1$, and another from stable *double-vortex* flow. Some evidence for such a splitting might be visible in our data for $Ra = 7 \times 10^9$ (figure 6*g*,*h*). This would be analogue to the separation of the *single-vortex* maximum from the *double-vortex* maximum with increasing Ra (figure 6). To verify this hypothesis, either a much finer sampling in Ro^{-1} and Γ^{-1} or another set at a larger Ra is necessary, which both are beyond the computational resources of this study.

The *single-vortex* maximum emerges with increasing Ra (figure 6). The regime of *single-vortex* flow is still very limited for $Ra = 2 \times 10^8$ and enlarges significantly with increasing Ra. For $Ra \geqslant 7 \times 10^8$ the sub-regime of *single-vortex* flow has sufficiently enlarged to form an individual maximum within our parameter sampling. Still, we can define the *single-vortex* maximum for $Ra = 2 \times 10^8$ based on the location of the most stable *single-vortex* flow at $\Gamma^{-1} = 6$, $Ro^{-1} \approx 16$ (Appendix B: figure 14*c*). However, it seems likely that the *single-vortex* flow is associated with larger Ra, and does not occur at very low $Ra \ll 10^8$. With increasing Ra and an enlarging *single-vortex* regime the enhancement efficiency of its maximum increases up to $\approx$20 %, which is comparable to the *double-vortex* maximum at the larger Ra (figure 7*a*). Independent of Ra, the *single-vortex* flow is limited to relatively strong confinement $\Gamma^{-1} > \Gamma^{-1}_{2VM}$, and occurs only for $\lambda_\Theta/\lambda_u > 1$ directly after the transition to the rotation-controlled regime (figure 8*c*,*f*). As shown before (§ 3.3, Appendix B: figure 11), this transition occurs gradually with extending periods in which the flow stays in a stable *single-vortex* state. Both *double-vortex* and *single-vortex* maxima shift towards faster rotation and stronger confinement for increasing Ra (figure 7*b*,*c*). Presumably, the locations of the maxima follow some effective scaling laws, but due to the large uncertainty we refrain from giving estimates for the scaling exponents.

The general trend of heat transport enhancement in wider vs slender cylinders, as already observed for $Ra = 7 \times 10^8$ (§ 4, figure 5), is present among all four Ra (figure 8*a*–*c*): in wider cylinders ($\Gamma^{-1} < \Gamma^{-1}_{2VM}(Ra)$), the rotation-controlled regime (blue symbols) begins at $\lambda_\Theta/\lambda_u \ll 1$, and we observe a nearly symmetric heat transport enhancement around $\lambda_\Theta/\lambda_u = 1$ (figure 8*a*,*d*). For $\Gamma^{-1}_{2VM}(Ra)$, the onset of heat transport enhancement occurs at $\lambda_\Theta/\lambda_u \approx 1$ and can be rather steep because the flow can immediately form a *double-vortex* structure as observed for lower Ra (figure 8*b*,*e*). In slender cylinders ($\Gamma^{-1} > \Gamma^{-1}_{2VM}(Ra)$), the heat transport enhancement always shows a sharp onset at $\lambda_\Theta/\lambda_u > 1$, which corresponds to an immediate transition from buoyancy-dominated regime to rotation-controlled regime with *single-vortex* flow (figure 8*c*,*f*). This representation of our data nicely depicts a Ra-independent clustering of the heat transport within the different flow regimes (figure 8*d*–*f*).

Collapsing all data into one frame emphasizes even better a sheet-like clustering (figure 10), which nicely illustrates the superposing character of both enhancing effects. In the buoyancy-dominated regime (grey symbols), no heat transport enhancement by rotation is observed among all combinations of Γ^{-1}, Ro^{-1} and Ra, and all enhancement is related to the *confinement* maximum, which collapses at $\lambda_\Theta/\lambda_u \approx 0.6$ for all Ra (see also § 4). Only when the azimuthal motion becomes predominant does Ekman pumping set in and enhance the heat transport (blue symbols). Thereby, the net enhancement and the resulting heat transport depend on the actual ratio between the kinetic and thermal

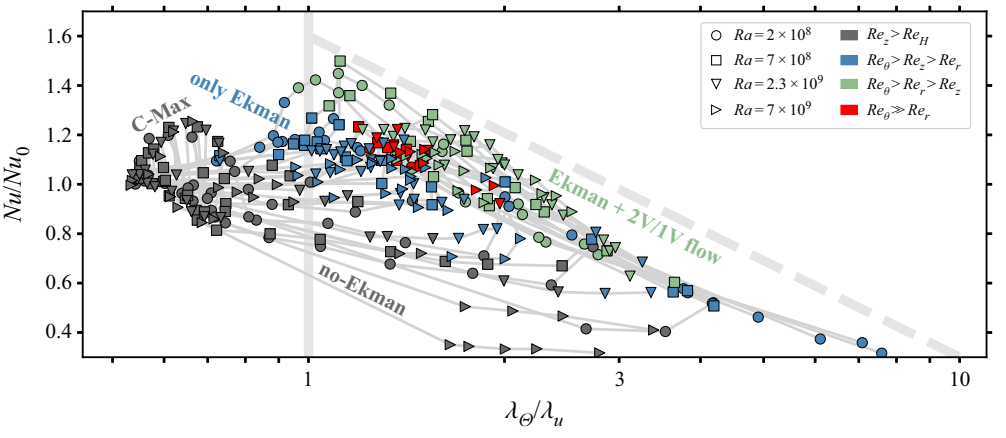

Figure 10. Clustering of the heat transport Nu/Nu_0 mapped onto the ratio of thermal and kinetic boundary layers λ_Θ/λ_u for all combinations of Ro^{-1}, Γ^{-1} and Ra. The data are coloured in the corresponding regimes of flow motion (figure 6): grey – without Ekman pumping, blue – with Ekman pumping, green and red – Ekman pumping and *double-vortex* or *single-vortex* flow. The vertical grey line marks the most beneficial boundary layer ratio $\lambda_\Theta/\lambda_u = 1$. The dashed grey line (no specific scaling) serves as guide for the eye. The grey lines connecting the data points follow increasing rotation Ro^{-1} per confinement Γ^{-1}.

boundary layer thicknesses. When additionally a *double-vortex* or *single-vortex* flow is present, the heat transport is further increased (green and red symbols) above the cases when only Ekman pumping is present. Thereby, *single-vortex* flow seems to be very limited to a much smaller interval of λ_Θ/λ_u than *double-vortex* flow. Whether Ekman pumping is active, and whether a (stable) domain-spanning flow is formed in addition depends on the combination of Ra, Γ^{-1}, Ro^{-1} and likely Pr that was not varied in this study. In other words: although a Ra-independent clustering is observed, several parameter values (e.g. larger Ra) can inhibit the best interference of a beneficial boundary layer ratio and a stable vortex flow, such that the largest potential heat transport enhancement is not achievable.

For all Ra, the onset of heat transport enhancement is nicely described by the transition of predominant fluid motion from vertical to horizontal $Re_z = Re_H$ (figures 6, 8). This transition and the onset of heat transport enhancement clearly depend on Ra, in contrast to describing the onset by a Ra-independent Ginzburg–Landau model (Weiss *et al.* 2010; Weiss & Ahlers 2011*a*,*b*). Nonetheless, a Ra-dependence in very confined systems seems meaningful regarding that the formation of horizontally dominated, vortical flow requires a sufficiently wide domain, larger than the most unstable convective length scale $L_c \propto Ek^{1/3} \propto Ra^{1/6}$. However, the Ra-dependence appears to be rather complex so that its complete derivation is beyond the scope of this study.

6. Conclusions

We have performed DNSs of confined-rotating RBC. For fixed Ra and Pr, we identified three distinct maxima in the parameter space of rotation Ro^{-1} and confinement Γ^{-1}: a *confinement*, a *double-vortex* and a *single-vortex* maximum. Each maximum can be linked to a regime with an individual characteristic domain-spanning flow structure. We find that the heat transport enhancement of these maxima can be explained by an interference of two effects:

(i) Heat injection: in the rotation-controlled regime of predominant vortical (horizontal) fluid motion and Ekman pumping, a beneficial ratio of thermal and kinetic boundary layer thicknesses $\lambda_\Theta/\lambda_u \approx 1$ leads to the most effective heat transport from the boundary layer *into* the bulk.

(ii) Bulk transport: certain combinations of rotation Ro^{-1}, confinement Γ^{-1} and thermal driving Ra trigger a stable domain-spanning flow formation, which supports effective heat transport *through* the bulk.

The interference of both enhancing effects in the (Ro^{-1}, Γ^{-1}) parameter space can result in one strong heat transport maximum, or cause a broad region of enhanced heat transport with multiple maxima. At lower $Ra \lesssim 2 \times 10^9$, a strong interference of both effects results in a larger heat transport enhancement for combined rotation and confinement than only confinement or only rotation could achieve. Contrary, at larger $Ra \gtrsim 2 \times 10^9$, where the interference is weak, pure confinement achieves the largest heat transport enhancement. Additionally, we have shown that the heat transport in strongly confined-rotating RBC does not automatically benefit from the optimal ratio of boundary layer thicknesses $\lambda_\Theta/\lambda_u \approx 1$, as it does not necessarily coincide with the presence of Ekman pumping, which is required for the enhancement.

Further investigations should aim to understand the occurrence of the different regimes of stable vortex formation for the various values of control parameters Γ^{-1}, Ro^{-1}, Ra and Pr, e.g. those for conditions in potential technical applications. Especially, understanding the onset of heat transport enhancement and the transition from buoyancy-dominated to rotation-controlled regime $Ro^{-1}_{BD\text{-}RC}(\Gamma^{-1}, Ra, Pr)$ promises further fundamental insights into the interplay of confinement and rotation. A better understanding of the general interaction of different types of stabilization remains important in various scientific fields such as geo- or astrophysics. This requires comparable studies on other combinations of interacting types of stabilization, e.g. rotating double-diffusive convection, confined double-diffusive convection or rotating magnetohydrodynamics.

Acknowledgements. We acknowledge the access to several computational resources, all of which were used for this work: PRACE for awarding us access to MareNostrum 4 based in Spain at the Barcelona Computing Center (BSC) under projects 2018194742 and 2020225335, the national e-infrastructure of SURFsara, a subsidiary of SURF cooperation, the collaborative ICT organization for Dutch education and research and NWO Science for the use of supercomputer facilities.

Funding. This work was funded by the ERC Starting Grant *UltimateRB* no. 804283.

Declaration of interests. The authors report no conflict of interest.

Data availability statement. The data that support the findings of this study are openly available in *4TU.ResearchData* at http://doi.org/10.4121/16974109.

Author ORCIDs.
Robert Hartmann https://orcid.org/0000-0002-4860-0449;
Roberto Verzicco https://orcid.org/0000-0002-2690-9998;
Detlef Lohse https://orcid.org/0000-0003-4138-2255;
Richard J.A.M. Stevens https://orcid.org/0000-0001-6976-5704.

Appendix A. Overview numerical simulations

Table 1 summarizes the most relevant details of the conducted numerical simulations.

Γ^{-1}	N_z	N_r	N_ϑ	M_{Ro}	Ro^{-1}	Nu_{max}	$N_{BL,min}$	$\left(\frac{\Delta z}{\eta}\right)_{mid}$	$\left(\frac{\Delta z}{\eta}\right)_{BL}$	Δt_{avg}	CFL_{max}	Δt_{max} (10^{-3})
$Ra = 2 \times 10^8$:												
2	256	64	384	10	0–33.$\bar{3}$	47.4	10	0.77	0.32	400	1.1	5
3	256	48	256	11	0–33.$\bar{3}$	57.0	8	0.79	0.40	400	1.1	5
4	256	32	192	12	0–33.$\bar{3}$	58.1	8	0.81	0.40	400	1.1	5
5	256	32	192	11	0–33.$\bar{3}$	46.6	10	0.87	0.42	400	0.4	5
6	256	32	192	11	0–33.$\bar{3}$	47.5	10	0.86	0.42	400	0.4	5
7	256	32	192	11	0–33.$\bar{3}$	48.0	10	0.83	0.32	100–400	0.4	5
8	256	32	192	11	0–33.$\bar{3}$	47.8	10	0.84	0.29	100–400	0.4	5
10	256	32	192	5	0–33.$\bar{3}$	43.9	10	0.82	0.24	400	0.4	5
$Ra = 7 \times 10^8$:												
3	384	64	384	10	0–33.$\bar{3}$	68.1	9	0.77	0.42	400	1.1	5
4	384	48	288	10	0–33.$\bar{3}$	76.0	9	0.78	0.50	1600	1.1	5
5	384	40	240	12	0–33.$\bar{3}$	85.8	8	0.79	0.53	1600	0.4	5
6	384	36	192	12	0–33.$\bar{3}$	74.5	9	0.84	0.56	1600	0.4	5
7	384	36	180	7	0–33.$\bar{3}$	66.7	10	0.88	0.56	400–1600	0.4	5
8	384	32	144	12	0–33.$\bar{3}$	66.4	10	0.88	0.56	400–1600	0.4	5
10	384	32	120	12	0–33.$\bar{3}$	71.5	9	0.83	0.41	400–1600	0.4	5
12	384	28	96	2	0–3.$\bar{3}$	71.6	9	0.85	0.22	400–1600	0.4	5
14	384	24	90	2	0–3.$\bar{3}$	68.2	9	0.83	0.20	400–1600	0.4	5
$Ra = 2.3 \times 10^9$:												
4	512	64	384	10	0–33.$\bar{3}$	95.9	10	0.87	0.45	400–1600	1.1	5
5	512	54	324	5	8–20	101.5	17	0.92	0.19	1600	1.1	5
6	512	48	256	13	0–33.$\bar{3}$	101.9	17	0.91	0.37	400–1600	1.1	5
7	512	48	240	9	10–33.$\bar{3}$	100.8	17	0.93	0.21	1600–3600	0.4	5
8	512	40	192	12	0–40	98.7	17	0.99	0.54	400–3600	0.4	5
9	512	40	180	7	12.5–28.6	99.1	17	1.06	0.24	1600–5600	0.4	5
10	512	36	160	11	0–40	101.0	17	1.06	0.24	400–1600	0.4	5
12	512	32	128	10	0–40	97.2	17	0.99	0.22	1600	0.4	5
14	512	30	120	6	0–40	101.0	17	1.00	0.15	1600	0.4	5
16	512	28	96	2	0–3.$\bar{3}$	103.6	16	1.02	0.08	1600	0.4	5
18	512	28	96	2	0–3.$\bar{3}$	101.3	17	1.01	0.08	1600	0.4	5
20	512	24	80	2	0–3.$\bar{3}$	96.9	17	0.98	0.07	1600	0.4	5
$Ra = 7 \times 10^9$:												
6	768	64	384	10	3.$\bar{3}$–25	128.3	24	0.90	0.14	1000–1800	0.4	1.5
7	768	60	360	10	3.$\bar{3}$–25	131.9	23	0.90	0.14	1200–2000	0.4	3
8	768	60	360	12	3.$\bar{3}$–33.$\bar{3}$	132.4	23	0.90	0.15	1200–2000	0.3	3
10	768	54	324	10	10–40	131.9	23	0.91	0.15	400–3600	0.4	2
12	768	48	288	6	20–40	133.7	23	1.02	0.17	1600–2800	0.4	2
16	768	40	240	8	0–40	130.0	24	0.94	0.16	400–1600	0.4	5
20	768	36	216	6	0–40	141.6	22	0.98	0.09	400–1600	0.4	5
24	768	32	192	7	0–33.$\bar{3}$	146.5	22	0.99	0.06	400–1600	0.2	4
28	768	30	180	2	0–3.$\bar{3}$	131.6	23	0.95	0.05	400–1600	0.4	3
32	768	28	162	2	0–3.$\bar{3}$	113.2	21	0.92	0.08	400	0.4	5

Table 1. Summary of numerical parameters per set of simulations (varying Ro^{-1}). Columns from left to right: confinement Γ^{-1}, number of grid points in the vertical, radial, azimuthal directions N_z, N_r, N_ϑ, number of simulations M_{Ro} per set, range of Ro^{-1} per set, largest Nusselt number Nu_{max} within each set, minimal number of points within the boundary layer $N_{BL,min}$ based on the estimate $\lambda_\Theta = 1/(2Nu_{max})$, coarsest resolution of the Kolmogorov scales η in the bulk $(\Delta z/\eta)_{mid}$, coarsest resolution of the Kolmogorov scales η in the boundary layers $(\Delta z/\eta)_{BL}$, averaging time interval Δt_{avg} in units of free-fall time (multiple values denote minimum and maximum value), maximal Courant number CFL_{max} and maximal time step Δt_{max} in units of free-fall time, both controlling the dynamic time stepping.

Appendix B. Supporting figures

Figure 11 shows the two (temporary) stable configurations of *single-vortex* flow in the vicinity around the stable *single-vortex* maximum. Figure 12 justifies that, for confined-rotating RBC, the change of predominant direction of flow motion from vertical to horizontal characterizes the onset of heat transport enhancement better than the transition of the kinetic boundary layer from Prandtl–Blasius to Ekman type. We note that in this context any Ekman pumping related increase of Nu with Ro^{-1} is seen as heat transport enhancement independent of whether $Nu/Nu_0 > 1$ or not. Figure 13 shows how kinetic and thermal boundary layer thicknesses evolve individually in the (Ro^{-1}, Γ^{-1}) parameter space. The kinetic boundary layer thickness λ_u is estimated as twice the height of the peak location of the horizontally averaged quantity $\langle \boldsymbol{u} \cdot \nabla^2 \boldsymbol{u} \rangle_H$. The thermal boundary layer thickness λ_Θ is defined as the intersection between the temperature gradient at the plate with a linear fit to the horizontally averaged mean temperature profile in the bulk, see also § 2. Figure 14 gives an overview on the additional flow characteristics (as in figure 1*c–e* for $Ra = 7 \times 10^8$) for all four Ra numbers.

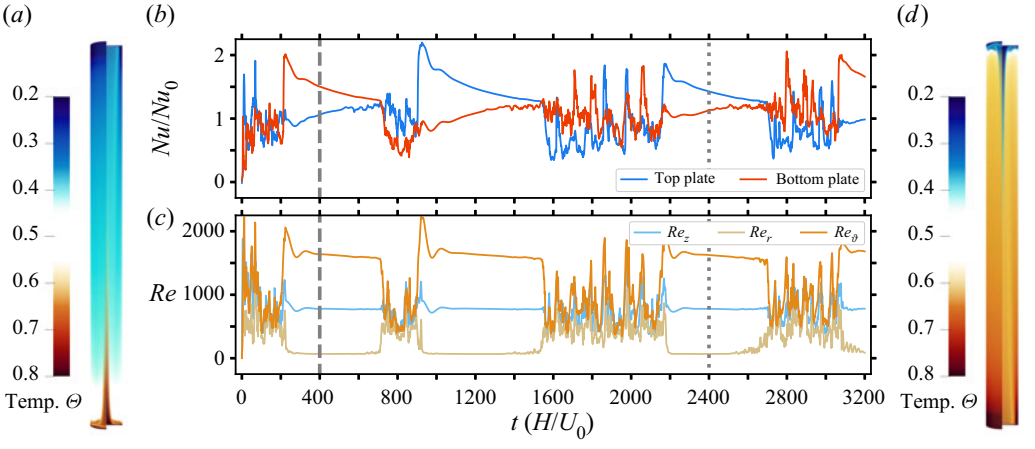

Figure 11. Configurations of *single-vortex* flow ($Ra = 7 \times 10^9$, $\Gamma^{-1} = 12$, $Ro^{-1} = 25$): (*a*) snapshot of the temperature field at $t = 400$ with a hot centred vortex, (*d*) snapshot of the temperature field at $t = 2400$ with a cold centred vortex, (*b*) temporal evolution of $Nu(t)$ at the top and bottom plates, (*c*) temporal evolution of $Re(t)$ for each velocity component. The vertical dashed and dotted lines indicate the times of the temperature snapshots in (*a*,*d*), respectively.

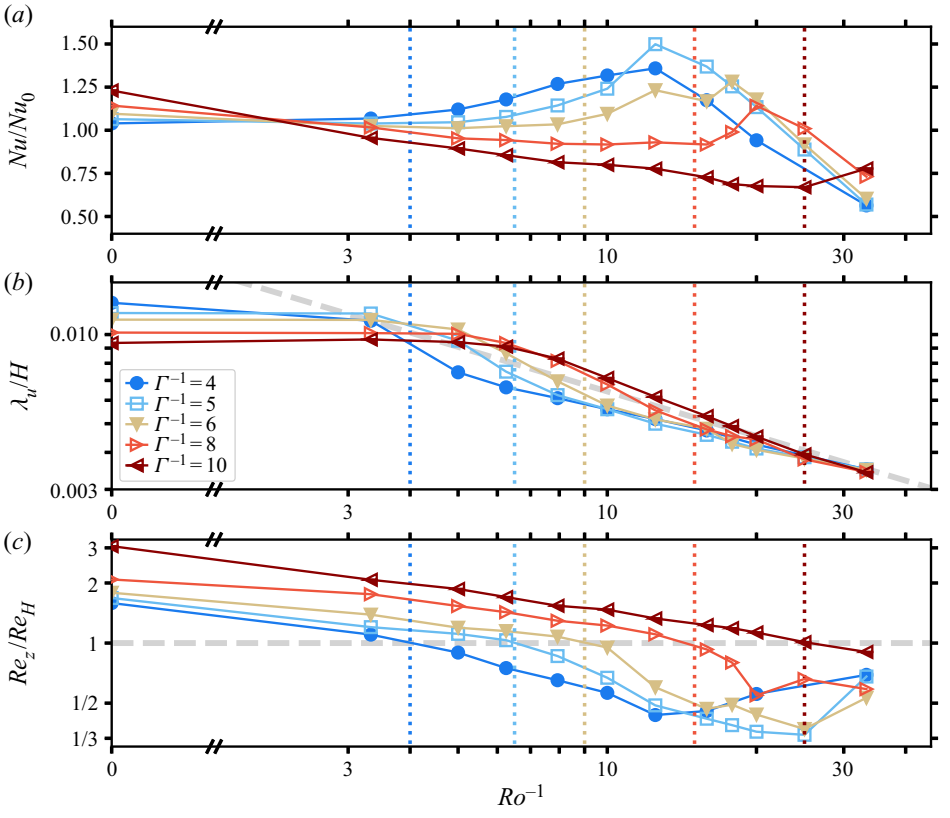

Figure 12. Onset of heat transport enhancement at $Ra = 7 \times 10^8$, $Pr = 4.38$: (*a*) normalized heat transport Nu/Nu_0 for various Γ^{-1}, (*b*) kinetic boundary layer thickness λ_u/H, the dashed grey line indicates Ekman type scaling $\lambda_u \propto 2.284((Pr/Ra)^{1/2}Ro)^{-1/2}$ (see Rajaei *et al.* 2016*a*), (*c*) ratio of vertical and horizontal Reynolds number Re_z/Re_H. The dashed grey line separates the regimes of predominant vertical ($Re_z/Re_H > 1$) and horizontal motion ($Re_z/Re_H < 1$). The vertical dotted lines indicate when $Re_z/Re_H = 1$ for each Γ^{-1}. In comparison this corresponds better with the onset of Ekman pumping enhanced heat transport (*a*) than the transition of the kinetic boundary layer from Prandtl–Blasius to Ekman type (*b*).

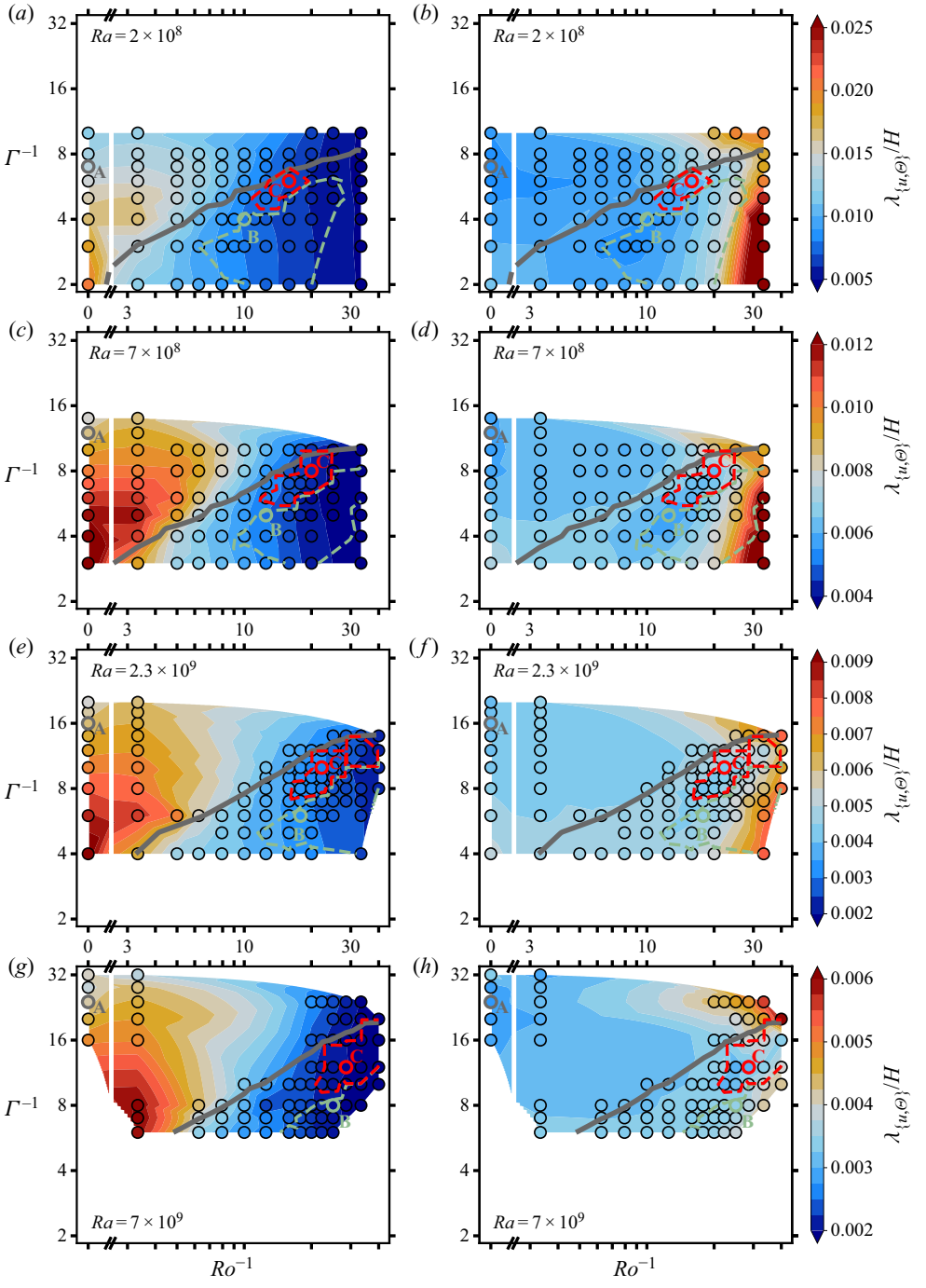

Figure 13. Boundary layer thicknesses in the (Ro^{-1}, Γ^{-1}) parameter space for (*a*,*b*) $Ra = 2 \times 10^8$, (*c*,*d*) $Ra = 7 \times 10^8$, (*e*,*f*) $Ra = 2.3 \times 10^9$, (*g*–*h*) $Ra = 7 \times 10^9$. (*a*,*c*,*e*,*g*) Kinetic boundary layer thickness λ_u/H. (*b*,*d*,*f*,*h*) Thermal boundary layer thickness λ_Θ/H. Each colour scale applies to both panels per *Ra*. The grey, green and red lines and highlighted locations A, B, C mark the regime transitions and heat transport maxima as in figure 6.

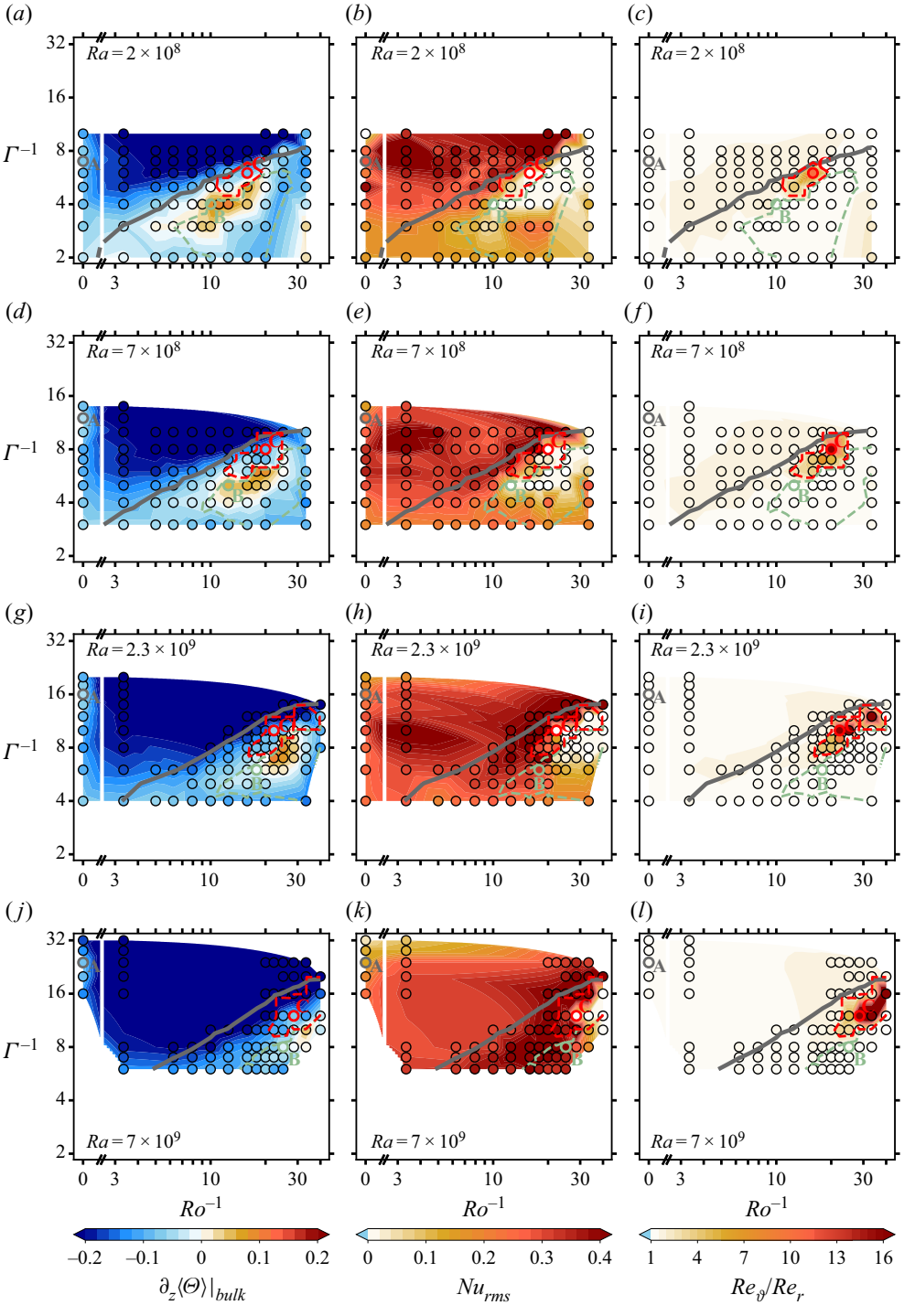

Figure 14. Additional flow characteristics for (*a–c*) $Ra = 2 \times 10^8$, (*d–f*) $Ra = 7 \times 10^8$, (*g–i*) $Ra = 2.3 \times 10^9$, (*j–l*) $Ra = 7 \times 10^9$. (*a*,*d*,*g*,*j*) Vertical temperature gradient in the bulk. (*b*,*e*,*h*,*k*) Temporal stability of the flow based on Nu_{rms} (2.5). (*c*,*f*,*i*,*l*) Ratio of azimuthal to radial Reynolds numbers Re_ϑ/Re_r. See figure 1(*c–e*) for detailed description.

References

Ahlers, G. *et al.* 2022 Aspect ratio dependence of heat transfer in a cylindrical Rayleigh-Bénard cell. *Phys. Rev. Lett.* **128**, 084501.

Ahlers, G., Grossmann, S. & Lohse, D. 2009 Heat transfer and large scale dynamics in turbulent Rayleigh–Bénard convection. *Rev. Mod. Phys.* **81**, 503–537.

Alards, K.M.J., Kunnen, R.P.J., Stevens, R.J.A.M., Lohse, D., Toschi, F. & Clercx, H.J.H. 2019 Sharp transitions in rotating turbulent convection: Lagrangian acceleration statistics reveal a second critical Rossby number. *Phys. Rev. Fluids* **4**, 074601.

Aurnou, J.M., Calkins, M.A., Cheng, J.S., Julien, K., King, E.M., Nieves, D., Soderlund, K.M. & Stellmach, S. 2015 Rotating convective turbulence in Earth and planetary cores. *Phys. Earth Planet. Inter.* **246**, 52–71.

Brown, E. & Ahlers, G. 2007 Temperature gradients, and search for non-Boussinesq effects, in the interior of turbulent Rayleigh–Bénard convection. *Europhys. Lett.* **80**, 14001.

Brown, E., Nikolaenko, A. & Ahlers, G. 2005 Reorientation of the large-scale circulation in turbulent Rayleigh–Bénard convection. *Phys. Rev. Lett.* **95**, 084503.

Buell, J.C. & Catton, I. 1983 Effect of rotation on the stability of a bounded cylindrical layer of fluid heated from below. *Phys. Fluids* **26** (4), 892–896.

Catton, I. & Edwards, D.K. 1970 Initiation of thermal convection in finite right circular cylinders. *AIChE J.* **16** (4), 594–601.

Chandrasekhar, S. 1961 *Hydrodynamic and Hydromagnetic Stability*. Oxford University Press.

Chilla, F. & Schumacher, J. 2012 New perspectives in turbulent Rayleigh–Bénard convection. *Eur. Phys. J.* E **35**, 58.

Chong, K.L., Huang, S.-D., Kaczorowski, M. & Xia, K.-Q. 2015 Condensation of coherent structures in turbulent flows. *Phys. Rev. Lett.* **115**, 264503.

Chong, K.L. & Xia, K.-Q. 2016 Exploring the severely confined regime in Rayleigh–Bénard convection. *J. Fluid Mech.* **805**, R4.

Chong, K.L., Yang, Y., Huang, S.-D., Zhong, J.-Q., Stevens, R.J.A.M., Verzicco, R., Lohse, D. & Xia, K.-Q. 2017 Confined Rayleigh–Bénard, rotating Rayleigh–Bénard, and double diffusive convection: a unifying view on turbulent transport enhancement through coherent structure manipulation. *Phys. Rev. Lett.* **119** (6), 064501.

Ecke, R.E. & Niemela, J.J. 2014 Heat transport in the geostrophic regime of rotating Rayleigh–Bénard convection. *Phys. Rev. Lett.* **113**, 114301.

Favier, B. & Knobloch, E. 2020 Robust wall states in rapidly rotating Rayleigh–Bénard convection. *J. Fluid Mech.* **895**, R1.

Glatzmaier, G.A. & Roberts, P.H. 1995 A three-dimensional self-consistent computer simulation of a geomagnetic field reversal. *Nature* **377**, 203–209.

Grossmann, S. & Lohse, D. 2000 Scaling in thermal convection: a unifying view. *J. Fluid Mech.* **407**, 27–56.

Grossmann, S. & Lohse, D. 2001 Thermal convection for large Prandtl number. *Phys. Rev. Lett.* **86**, 3316–3319.

Hartmann, D.L., Moy, L.A. & Fu, Q. 2001 Tropical convection and the energy balance at the top of the atmosphere. *J. Clim.* **14**, 4495–4511.

Hartmann, R., Chong, K.L., Stevens, R.J.A.M., Verzicco, R. & Lohse, D. 2021 Heat transport enhancement in confined Rayleigh–Bénard convection feels the shape of the container. *Europhys. Lett.* **135** (2), 24004.

Heimpel, M., Aurnou, J. & Wicht, J. 2005 Simulation of equatorial and high-latitude jets on Jupiter in a deep convection model. *Nature* **438**, 193–196.

Huang, S.D., Kaczorowski, M., Ni, R. & Xia, K.-Q. 2013 Confinement-induced heat-transport enhancement in turbulent thermal convection. *Phys. Rev. Lett.* **111** (10), 104501.

Julien, K., Legg, S., McWilliams, J. & Werne, J. 1996 Rapidly rotating Rayleigh–Bénard convection. *J. Fluid Mech.* **322**, 243–273.

Julien, K., Rubio, A.M., Grooms, I. & Knobloch, E. 2012 Statistical and physical balances in low Rossby number Rayleigh–Bénard convection. *Geophys. Astrophys. Fluid Dyn.* **106**, 392–428.

King, E.M., Stellmach, S., Noir, J., Hansen, U. & Aurnou, J.M. 2009 Boundary layer control of rotating convection systems. *Nature* **457**, 301.

Kooij, G.L., Botchev, M.A., Frederix, E.M.A., Geurts, B.J., Horn, S., Lohse, D., van der Poel, E.P., Shishkina, O., Stevens, R.J.A.M. & Verzicco, R. 2018 Comparison of computational codes for direct numerical simulations of turbulent Rayleigh–Bénard convection. *Comput. Fluids* **166**, 1–8.

KUNNEN, R.P.J., CLERCX, H.J.H. & GEURTS, B.J. 2006 Heat flux intensification by vortical flow localization in rotating convection. *Phys. Rev.* E **74**, 056306.

KUNNEN, R.P.J., CLERCX, H.J.H. & GEURTS, B.J. 2008 Breakdown of large-scale circulation in turbulent rotating convection. *Europhys. Lett.* **84**, 24001.

KUNNEN, R.P.J., OSTILLA-MÓNICO, R., VAN DER POEL, E.P., VERZICCO, R. & LOHSE, D. 2016 Transition to geostrophic convection: the role of the boundary conditions. *J. Fluid Mech.* **799**, 413–432.

KUNNEN, R.P.J., STEVENS, R.J.A.M., OVERKAMP, J., SUN, C., VAN HEIJST, G.J.F. & CLERCX, H.J.H. 2011 The role of Stewartson and Ekman layers in turbulent rotating Rayleigh–Bénard convection. *J. Fluid Mech.* **688**, 422–442.

LIU, Y. & ECKE, R.E. 1997 Heat transport scaling in turbulent Rayleigh–Bénard convection: effects of rotation and Prandtl number. *Phys. Rev. Lett.* **79**, 2257–2260.

LOHSE, D. & XIA, K.-Q. 2010 Small-scale properties of turbulent Rayleigh–Bénard convection. *Annu. Rev. Fluid Mech.* **42**, 335–364.

LU, H.-Y., DING, G.-Y., SHI, J.-Q., XIA, K.-Q. & ZHONG, J.-Q. 2021 Heat-transport scaling and transition in geostrophic rotating convection with varying aspect ratio. *Phys. Rev. Fluids* **6**, L071501.

NIEVES, D., RUBIO, A.M. & JULIEN, K. 2014 Statistical classification of flow morphology in rapidly rotating Rayleigh–Bénard convection. *Phys. Fluids* **26**, 086602.

VAN DER POEL, E.P., OSTILLA-MÓNICO, R., DONNERS, J. & VERZICCO, R. 2015 A pencil distributed finite difference code for strongly turbulent wall-bounded flows. *Comput. Fluids* **116**, 10–16.

PROUDMAN, J. 1916 On the motion of solids in a liquid possessing vorticity. *Proc. R. Soc. Lond.* A **92**, 408–424.

RADKO, T. 2013 *Double-Diffusive Convection*. Cambridge University Press.

RAJAEI, H., JOSHI, P., ALARDS, K.M.J., KUNNEN, R.P.J., TOSCHI, F. & CLERCX, H.J.H. 2016*a* Transitions in turbulent rotating convection: a Lagrangian perspective. *Phys. Rev.* E **93**, 043129.

RAJAEI, H., JOSHI, P., KUNNEN, R.P.J. & CLERCX, H.J.H. 2016*b* Flow anisotropy in rotating buoyancy-driven turbulence. *Phys. Rev. Fluids* **1**, 044403.

ROSSBY, H.T. 1969 A study of Bénard convection with and without rotation. *J. Fluid Mech.* **36**, 309–335.

SCHMITT, R.W., LEDWELL, J.R., MONTGOMERY, E.T., POLZIN, K.L. & TOOLE, J.M. 2005 Enhanced diapycnal mixing by salt fingers in the thermocline of the tropical atlantic. *Science* **308** (5722), 685–688.

SHISHKINA, O., STEVENS, R.J.A.M., GROSSMANN, S. & LOHSE, D. 2010 Boundary layer structure in turbulent thermal convection and its consequences for the required numerical resolution. *New J. Phys.* **12**, 075022.

SPRAGUE, M., JULIEN, K., KNOBLOCH, E. & WERNE, J. 2006 Numerical simulation of an asymptotically reduced system for rotationally constrained convection. *J. Fluid Mech.* **551**, 141–174.

STELLMACH, S., LISCHPER, M., JULIEN, K., VASIL, G., CHENG, J.S., RIBEIRO, A., KING, E.M. & AURNOU, J.M. 2014 Approaching the asymptotic regime of rapidly rotating convection: boundary layers versus interior dynamics. *Phys. Rev. Lett.* **113**, 254501.

STEVENS, R.J.A.M., CLERCX, H.J.H. & LOHSE, D. 2010*a* Boundary layers in rotating weakly turbulent Rayleigh–Bénard convection. *Phys. Fluids* **22**, 085103.

STEVENS, R.J.A.M., CLERCX, H.J.H. & LOHSE, D. 2010*b* Optimal Prandtl number for heat transfer in rotating Rayleigh–Bénard convection. *New J. Phys.* **12**, 075005.

STEVENS, R.J.A.M., CLERCX, H.J.H. & LOHSE, D. 2012 Breakdown of the large-scale wind in aspect ratio $\Gamma = 1/2$ rotating Rayleigh–Bénard flow. *Phys. Rev.* E **86**, 056311.

STEVENS, R.J.A.M., CLERCX, H.J.H. & LOHSE, D. 2013*a* Heat transport and flow structure in rotating Rayleigh–Bénard convection. *Eur. J. Mech. (*B*/Fluids)* **40**, 41–49.

STEVENS, R.J.A.M., VAN DER POEL, E.P., GROSSMANN, S. & LOHSE, D. 2013*b* The unifying theory of scaling in thermal convection: the updated prefactors. *J. Fluid Mech.* **730**, 295–308.

STEVENS, R.J.A.M., ZHONG, J.-Q., CLERCX, H.J.H., AHLERS, G. & LOHSE, D. 2009 Transitions between turbulent states in rotating Rayleigh–Bénard convection. *Phys. Rev. Lett.* **103**, 024503.

TAYLOR, G.I. & LAMB, H. 1917 Motion of solids in fluids when the flow is not irrotational. *Proc. R. Soc. Lond.* A **93** (648), 99–113.

TILGNER, A., BELMONTE, A. & LIBCHABER, A. 1993 Temperature and velocity profiles of turbulence convection in water. *Phys. Rev.* E **47**, R2253–R2256.

TIMMERMANS, M.L., TOOLE, J., KRISHFIELD, R. & WINSOR, P. 2008 Ice-tethered profiler observations of the double-diffusive staircase in the Canada Basin thermocline. *J. Geophys. Res.* **113**, C00A02.

VERZICCO, R. & CAMUSSI, R. 1997 Transitional regimes of low-Prandtl thermal convection in a cylindrical cell. *Phys. Fluids* **9**, 1287–1295.

VERZICCO, R. & CAMUSSI, R. 1999 Prandtl number effects in convective turbulence. *J. Fluid Mech.* **383**, 55–73.

VERZICCO, R. & ORLANDI, P. 1996 A finite-difference scheme for three-dimensional incompressible flow in cylindrical coordinates. *J. Comput. Phys.* **123**, 402–413.

VOROBIEFF, P. & ECKE, R.E. 1998 Vortex structure in rotating Rayleigh–Bénard convection. *Physica* D **123**, 153–160.

WAGNER, S., SHISHKINA, O. & WAGNER, C. 2012 Boundary layers and wind in cylindrical Rayleigh–Bénard cells. *J. Fluid Mech.* **697**, 336–366.

WEI, P., WEISS, S. & AHLERS, G. 2015 Multiple transitions in rotating turbulent Rayleigh–Bénard convection. *Phys. Rev. Lett.* **114**, 114506.

WEISS, S. & AHLERS, G. 2011*a* Heat transport by turbulent rotating Rayleigh–Bénard convection and its dependence on the aspect ratio. *J. Fluid Mech.* **684**, 407–426.

WEISS, S. & AHLERS, G. 2011*b* The large-scale flow structure in turbulent rotating Rayleigh–Bénard convection. *J. Fluid Mech.* **688**, 461–492.

WEISS, S., STEVENS, R.J.A.M., ZHONG, J.-Q., CLERCX, H.J.H., LOHSE, D. & AHLERS, G. 2010 Finite-size effects lead to supercritical bifurcations in turbulent rotating Rayleigh–Bénard convection. *Phys. Rev. Lett.* **105**, 224501.

WEISS, S., WEI, P. & AHLERS, G. 2016 Heat-transport enhancement in rotating turbulent Rayleigh–Bénard convection. *Phys. Rev.* E **93**, 043102.

DE WIT, X.M., GUZMÁN, A.J.A., MADONIA, M., CHENG, J.S., CLERCX, H.J.H. & KUNNEN, R.P.J. 2020 Turbulent rotating convection confined in a slender cylinder: the sidewall circulation. *Phys. Rev. Fluids* **5** (2), 023502.

YANG, Y., VERZICCO, R., LOHSE, D. & STEVENS, R.J.A.M. 2020 What rotation rate maximizes heat transport in rotating Rayleigh–Bénard convection with Prandtl number larger than one? *Phys. Rev. Fluids* **5** (5), 053501.

ZHANG, X., ECKE, R.E. & SHISHKINA, O. 2021 Boundary zonal flows in rapidly rotating turbulent thermal convection. *J. Fluid Mech.* **915**, A62.

ZHANG, X., VAN GILS, D.P.M., HORN, S., WEDI, M., ZWIRNER, L., AHLERS, G., ECKE, R.E., WEISS, S., BODENSCHATZ, E. & SHISHKINA, O. 2020 Boundary zonal flow in rotating turbulent Rayleigh–Bénard convection. *Phys. Rev. Lett.* **124** (8), 084505.

ZHONG, F., ECKE, R.E. & STEINBERG, V. 1991 Asymmetric modes and the transition to vortex structures in rotating Rayleigh–Bénard convection. *Phys. Rev. Lett.* **67**, 2473–2476.

ZHONG, J.-Q., STEVENS, R.J.A.M., CLERCX, H.J.H., VERZICCO, R., LOHSE, D. & AHLERS, G. 2009 Prandtl-, Rayleigh-, and Rossby-number dependence of heat transport in turbulent rotating Rayleigh–Bénard convection. *Phys. Rev. Lett.* **102**, 044502.

ZWIRNER, L. & SHISHKINA, O. 2018 Confined inclined thermal convection in low-Prandtl-number fluids. *J. Fluid Mech.* **850**, 984–1008.